

1 Environmental changes during the onset of the Late Pliensbachian 2 Event (Early Jurassic) in the Cardigan Bay Basin, Wales.

3
4 Teuntje P. Hollaar^{1,2}, Stephen P. Hesselbo^{2,3}, Jean-François Deconinck⁴, Magret Damaschke⁵,
5 Clemens V. Ullmann^{2,3}, Mengjie Jiang², Claire M. Belcher¹.

6 1 WildFIRE Lab, Global Systems Institute, University of Exeter, Exeter, EX4 4PS, UK

7 2 Camborne School of Mines, Department of Earth and Environmental Sciences, University of Exeter, Penryn
8 Campus, Penryn, TR10 9FE, UK

9 3 Environment and Sustainability Institute, University of Exeter, Penryn Campus, Penryn, TR10 9FE, UK

10 4 Biogéosciences, UMR 6282 CNRS, Université de Bourgogne/Franche-Comté, 21000 Dijon, France

11 5 Core Scanning Facility, British Geological Survey, Keyworth, NG12 5GG, UK

12 *Correspondence to:* Teuntje P. Hollaar (t.p.hollaar@exeter.ac.uk)

13

14 **Abstract.** The Late Pliensbachian Event (LPE), in the Early Jurassic, is associated with a perturbation in the
15 global carbon cycle (positive carbon isotope excursion (CIE) of ~ 2 ‰), cooling of $\sim 5^\circ\text{C}$, and the deposition of
16 widespread regressive facies. Cooling during the Late Pliensbachian has been linked to enhanced organic matter
17 burial and/or disruption of thermohaline ocean circulation due to sea level lowstand of at least regional extent .
18 Orbital forcing had a strong influence on the Pliensbachian environments and recent studies show that the
19 terrestrial realm and the marine realm in and around the Cardigan Bay Basin, UK, were strongly influenced by
20 orbital climate forcing. In the present study we build on the previously published data for long eccentricity cycle
21 $E459 \pm 1$ and extend the palaeoenvironmental record to include $E458 \pm 1$. We explore the environmental and
22 depositional changes on orbital time scales for the Llanbedr (Mochras Farm) core during the onset of the LPE.
23 Clay mineralogy, XRF elemental analysis, isotope ratio mass spectrometry, and palynology are combined to
24 resolve systematic changes in erosion, weathering, fire, grain size and riverine influx. Our results indicate
25 distinctively different environments before and after the onset of the LPE positive CIE, and show increased
26 physical erosion relative to chemical weathering. We also identify five swings in the climate, in tandem with the
27 405 kyr eccentricity minima and maxima. Eccentricity maxima are linked to precessionally repeated
28 occurrences of a semi-arid monsoonal climate with high fire activity and relatively coarser sediment from
29 terrestrial runoff. In contrast, 405 kyr minima in the Mochras core are linked to a more persistent, annually wet
30 climate, low fire activity, and relatively finer grained deposits across multiple precession cycles. The onset of
31 the LPE +ve CIE did not impact the expression of the 405 kyr cycle in the proxy records; however, during the
32 second pulse of heavier carbon (^{13}C) enrichment, the clay minerals record a change from dominant chemical
33 weathering to dominant physical erosion.

34

35 1 Introduction

36 The Early Jurassic is a period marked by large climatic fluctuations and associated carbon-isotope excursions
37 (CIE's) in an overall warmer than present and high $p\text{CO}_2$ world (McElwain *et al.*, 2005; Korte and Hesselbo,
38 2011; Steinthorsdottir and Vajda, 2015; Korte *et al.*, 2015; Robinson *et al.*, 2016). A series of small and medium
39 sized CIE's have recently been documented for the Sinemurian and Pliensbachian, which have mainly been

40 from European, North African and North American records (Korte and Hesselbo, 2011; Franceschi *et al.*, 2014;
41 Korte *et al.*, 2015; Price *et al.*, 2016; De Lena *et al.*, 2019; Hesselbo *et al.*, 2020a; Mercuzot *et al.*, 2020; Storm
42 *et al.*, 2020; Silva *et al.*, 2021; Cifer *et al.*, 2022; Bodin *et al.*, 2023). Notable is the pronounced positive CIE in
43 the Late Pliensbachian, which has been called the Late Pliensbachian Event (LPE) and is linked to climatic
44 cooling (Hesselbo and Korte, 2011; Korte *et al.*, 2015) and a supra-regional/global sea level low stand (Hallam,
45 1981; de Graciansky *et al.*, 1998; Hesselbo and Jenkyns, 1998; Hesselbo, 2008). The LPE has been recognized
46 by a positive shift in benthic marine oxygen-isotopes (~1.5–2 per mil) (Bailey *et al.*, 2003; Rosales *et al.*,
47 2004,2006; Suan *et al.*, 2010; Dera *et al.*, 2011a; Korte and Hesselbo, 2011; Gómez *et al.*, 2016; Alberti *et al.*,
48 2019, 2021), coeval with a positive shift in marine and terrestrial carbon isotopes (~2 per mil) (Jenkyns and
49 Clayton, 1986; McArthur *et al.*, 2000; Morettini *et al.*, 2002; Quesada *et al.*, 2005; Rosales *et al.*, 2006; Suan *et al.*
50 *et al.*, 2010; Korte and Hesselbo, 2011; Silva *et al.*, 2011; Gómez *et al.*, 2016; De Lena *et al.*, 2019).

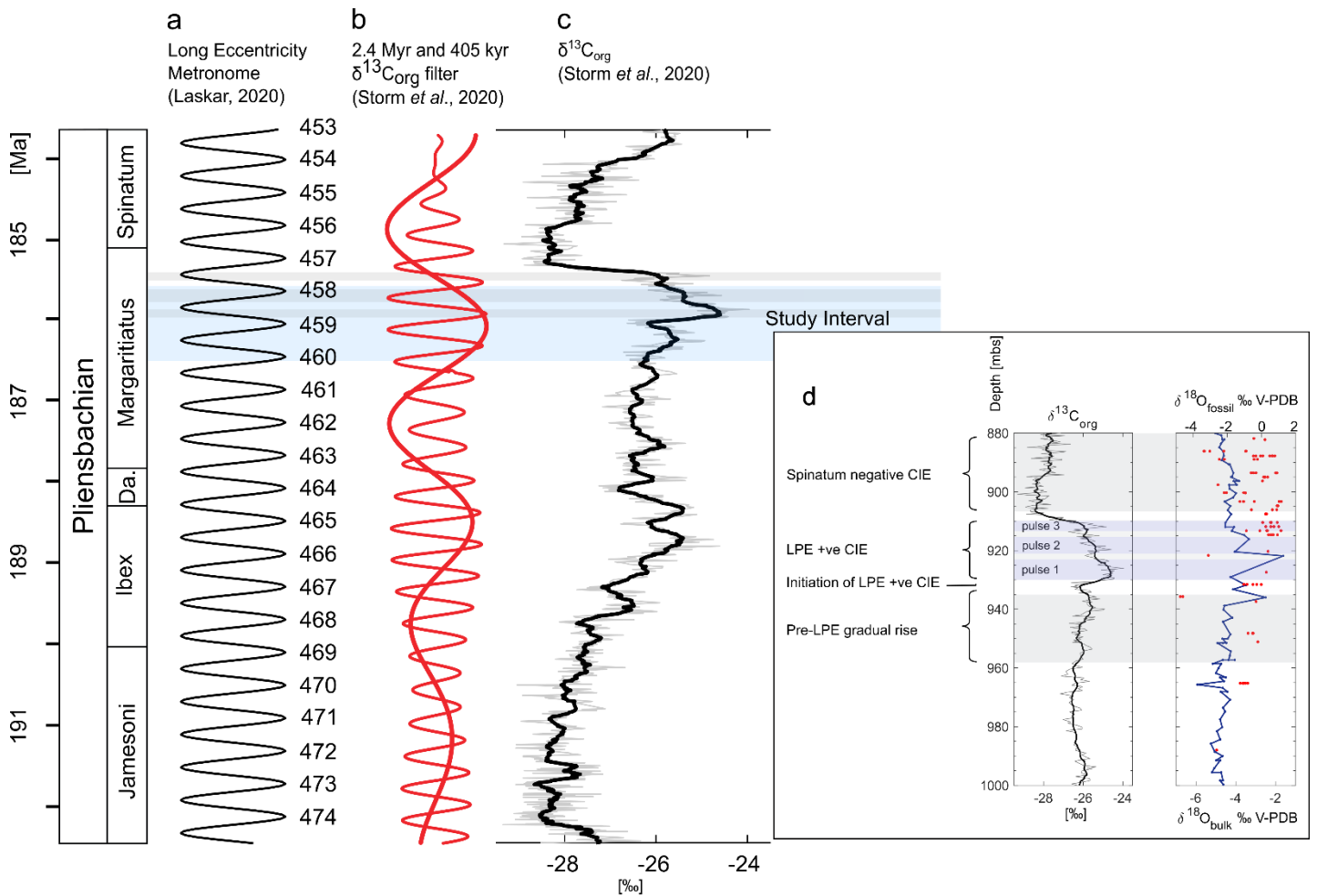
51 A cooler Late Pliensbachian climate has been suggested based on low $p\text{CO}_2$ values inferred by leaf stomatal
52 index data from eastern Australia (Steinthorsdottir and Vajda, 2015), the presence of glendonites in northern
53 Siberia (Kaplan, 1978; Price, 1999; Rogov and Zakharov, 2010), vegetation shifts from a diverse flora of
54 different plant groups to one mainly dominated by bryophytes in Siberia (Ilyina, 1985; Zakharov *et al.*, 2006),
55 and possible ice rafted debris found in Siberia (Price, 1999; Suan *et al.*, 2011). Whilst the presence of ice sheets
56 is strongly debated, a general cooling period (~5°C lower; Korte *et al.*, 2015; Gómez *et al.*, 2016) is evident
57 from several temperature reconstructions from NW Europe. A cooling is hypothesized via enhanced carbon
58 burial in the marine sediments, leading to lower $p\text{CO}_2$ values and initiating cooler climatic conditions (Jenkyns
59 and Clayton, 1986; Suan *et al.*, 2010; Silva *et al.*, 2011; Storm *et al.*, 2020). Direct evidence of large-scale
60 carbon burial in Upper Pliensbachian marine deposits has not yet been documented (Silva *et al.*, 2021).

61 Alternatively, cooling has been suggested to be caused by a lower sea level which would have disrupted ocean
62 circulation in the Laurasian Seaway, reducing poleward heat transport from the tropics (Korte *et al.*, 2015). In
63 the UK region, a dome structure in the North Sea has been linked to shedding of sediments during sea level low
64 stands from the Late Toarcian and possibly before (Underhill and Partington, 1993; Korte *et al.*, 2015; Archer *et al.*
65 2019). Disruption of the ocean circulation between the western Tethys and the Boreal realm is supported by
66 marine migration patterns (Schweigert, 2005; Zakharov *et al.*, 2006; Bourillot *et al.*, 2008; Nikitenko, 2008;
67 Dera *et al.*, 2011b; van de Schootbrugge *et al.*, 2019) and numerical models (Bjerrum *et al.*, 2001; Dera and
68 Donnadieu, 2012; Ruvalcaba Baroni *et al.* 2018); however, the net direction of the flows remain debated.

69 An additional factor to be considered is that a strong orbital control exists on the Pliensbachian sedimentary
70 successions (Weedon and Jenkyns, 1990; Ruhl *et al.*, 2016; Hinnov *et al.*, 2018; Storm *et al.*, 2020; Hollaar *et al.*
71 *et al.*, 2021). Previous studies have indicated that sea level changes, possibly coupled to glacio-eustatic rise and
72 fall, occurred during the LPE on a 100 kyr (short eccentricity) time scale (Korte and Hesselbo, 2011). A high-
73 resolution record of charcoal, clay mineralogy, bulk-organic carbon-isotopes, TOC and CaCO_3 encompassing
74 approximately one 405 kyr cycle from the Llanbedr (Mochras Farm) borehole, Cardigan Bay Basin, NW Wales,
75 UK, suggested that the long-eccentricity orbital cycle had a significant effect on background climatic and
76 environmental change during the late Pliensbachian, particularly affecting the hydrological regime of the region
77 (Hollaar *et al.*, 2021). This previous research focussed on orbital forcing of environmental change for a time
78 lacking any large excursion in $\delta^{13}\text{C}_{\text{org}}$, and so unaffected by perturbations to the global carbon cycle. Here, we

79 expand on the record of Hollaar *et al.* (2021) to cover two long eccentricity cycles (which we identify as
 80 spanning from cycle E459 \pm 1 to the start of E457 \pm 1 of Laskar *et al.* 2011 and Laskar 2020), where the final
 81 parts of E458 and the start of E457 are interrupted by onset of the Late Pliensbachian Event (Fig. 1). This longer
 82 record allows us to more robustly examine the influence of the long eccentricity cycle and the potential impact
 83 of a global carbon cycle perturbation on the palaeoclimate and depositional environment. We find that the long
 84 eccentricity forcing continued to dictate the precise timing of major environmental changes in the Cardigan Bay
 85 Basin, including the initial step of the positive carbon isotope excursion.

86



87 **Figure 1: Stratigraphic framework of the Mochras borehole.** (a) 405 kyr metronome (Laskar, 2020) which
 88 shows that this study spans E459 \pm 1 to E457 \pm 1. (b) 2.4 Myr and 405 kyr filter derived from the $\delta^{13}\text{C}_{\text{org}}$ record
 89 from Storm *et al.* (2020). A slight offset in pacing is observed in the 405 kyr metronome based on an assumed
 90 fixed 405 kyr cycle length (a), versus filtering of the 405 kyr signal from the orbital solution (b). (c) $\delta^{13}\text{C}_{\text{org}}$
 91 curve from the Mochras borehole (Storm *et al.*, 2020), showing the \sim 1.8 ‰ +CIE that marks the LPE. High
 92 resolution data are visualized in light grey and a 10-step moving average in black. The blue bar marks interval in
 93 the Mochras borehole considered in this study. The three grey shaded bars represent the three pulses in the +CIE
 94 of the LPE. (d) Close-up of the $\delta^{13}\text{C}_{\text{org}}$ (Storm *et al.*, 2020) and $\delta^{18}\text{O}_{\text{bulk}}$ and $\delta^{18}\text{O}_{\text{fossil}}$ (Ullmann *et al.*, 2022) from
 95 the Late Pliensbachian of the Mochras core. A pre-LPE gradual rise is recorded in the $\delta^{13}\text{C}_{\text{org}}$, followed by the
 96 initiation of the LPE +ve CIE, which consists of three pulses. After the LPE +ve CIE, $\delta^{13}\text{C}_{\text{org}}$ values drop

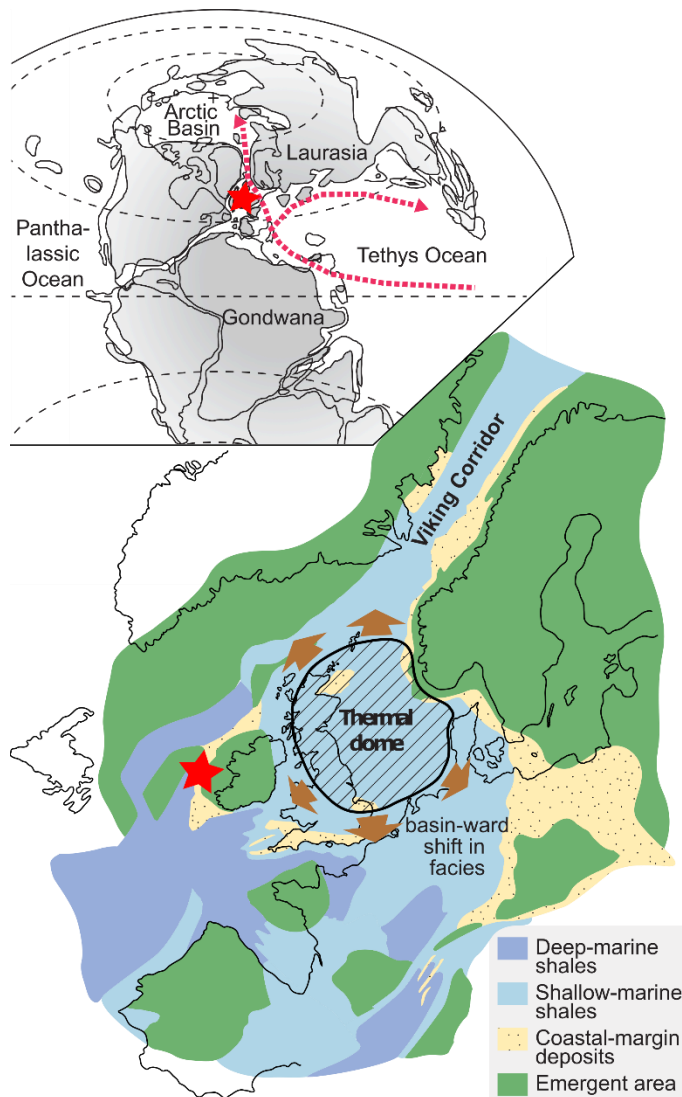
97 recorded starting at ~910 mbs, and the Spinatum negative CIE is recorded. The $\delta^{18}\text{O}_{\text{bulk}}$ of the Mochras core
98 (blue) is diagenetically altered and unlikely to preserve a palaeoclimatic imprint (Ullmann *et al.*, 2022). Also,
99 shown are $\delta^{18}\text{O}_{\text{fossil}}$ values (red).

100

101 **2 Material**

102 **2.1 Palaeo-location and setting**

103 Associated with the break-up of Pangea, connections between oceans via epicontinental seaways were
104 established during the Early Jurassic, such as the Hispanic Corridor, which connected the north-western Tethys
105 and the eastern Panthalassa, and the Viking Corridor which linked the north-western Tethys Ocean to the Boreal
106 Sea (Sellwood and Jenkyns, 1975; Smith *et al.*, 1983; Bjerrum *et al.*, 2001; Damborenea *et al.*, 2012). The
107 linking passage of the NW Tethys Ocean and the Boreal Sea (south of the Viking Corridor) is the
108 palaeogeographical location of the Llanbedr (Mochras Farm) borehole, Cardigan Bay Basin, NW Wales, UK
109 (Fig. 2) – referred to hereafter as Mochras. Due to the location of the Mochras succession during the Late
110 Pliensbachian, it was subject to both polar and equatorial influences allowing study of variations in the
111 circulation in the N-S Laurasian Seaway (including the Viking Corridor) prior to and across the LPE. Mochras
112 was located at a mid-palaeolatitude of ~35° N (cf. Torsvik and Cocks, 2017).



113

114 **Figure 2: Palaeolocation of the Mochras borehole in the context of potential North Sea doming.** Figure
 115 reprinted and adapted from Korte *et al.* (2015), which is open access
 116 (<https://creativecommons.org/licenses/by/4.0/>). The Mochras borehole was located at a paleolatitude of $\sim 35^\circ$ N
 117 in the Cardigan Bay Basin (Torsvik and Cocks, 2017). Circulation in the Tethys Ocean and between there and
 118 the Boreal region influenced the depositional environment of the Mochras core (Pieńkowski *et al.*, 2021). Late
 119 Pliensbachian sea level fall potentially resulted in occlusion of the Viking Corridor as the topography of the
 120 North Sea dome structure disrupted circulation in the seaway (Korte *et al.*, 2015).

121

122 The depositional environment of Mochras is likely characterized by a rift setting, which is reflected by the
 123 relatively open and deep marine facies and the evidence for below storm wave-base and contourite deposition
 124 (Pieńkowski *et al.*, 2021), but always with a strong terrestrial influence (van de Schootbrugge *et al.*, 2005;
 125 Riding *et al.*, 2013) from the nearby landmasses (Dobson and Whittington, 1987). The Cardigan Bay Basin fill
 126 was downthrown against the Early Paleozoic Welsh Massif by a major normal fault system, probably
 127 comprising the Bala, Mochras and Tonfanau faults at the eastern and south-eastern margins of the basin in Late
 128 Paleozoic–Early Mesozoic time (Woodland, 1971; Tappin *et al.*, 1994). The main source of detrital material is

129 understood to be the Caledonian Welsh Massif, followed by the Irish and Scottish landmasses (Deconinck *et al.*,
130 2019). Other massifs that could have influenced the provenance are the London-Brabant Massif to the south
131 east, and Cornubia to the south (van de Schootbrugge *et al.*, 2005), depending on the marine circulation and
132 sediment transport at the time.

133 **2.2 Core location and material**

134 The Llanbedr (Mochras Farm) Borehole was drilled onshore in the Cardigan Bay Basin (52° 48' 32" N, 4° 08' 44"
135 W) in 1967–1969, North Wales (Woodland, 1971; Hesselbo *et al.*, 2013). The borehole recovered a 1300 m
136 thick Early Jurassic sequence (601.83–1906.78 metres below surface (mbs)), yielding the most complete and
137 extended Early Jurassic succession in the UK, being double the thickness of same age strata in other UK cores
138 and outcrops (Hesselbo *et al.*, 2013; Ruhl *et al.*, 2016). The Lower Jurassic is biostratigraphically complete at
139 the zonal level (Ivimey-Cook, 1971; Copestake and Johnson, 2014), with the top truncated and unconformably
140 overlain by Cenozoic strata (Woodland, 1971; Dobson and Whittington, 1987; Tappin *et al.*, 1994; Hesselbo *et*
141 *al.*, 2013). The lithology is dominated by argillaceous sediments, with alternating muddy limestone, marl and
142 mudstone (Woodland, 1971; Sellwood and Jenkyns, 1975).

143 The Pliensbachian Stage in the Mochras borehole occurs between ~1250 and ~865 mbs, with the Margaritatus
144 Zone between ~1013 and 909 mbs (Page in Copestake and Johnson, 2014). The Pliensbachian interval
145 comprises alternations of mudstone (with a moderate total organic carbon [TOC]) and organic-poor limestones,
146 with a pronounced cyclicity at $\sim 1 \pm 0.5$ m wavelength (Ruhl *et al.*, 2016). The Upper Pliensbachian contains
147 intervals that are silty and locally sandy, whilst levels of relative organic enrichment also occur through the
148 Pliensbachian (Ruhl *et al.*, 2016). Overall, the Upper Pliensbachian is relatively rich in carbonate (Ruhl *et al.*,
149 2016; Ullmann *et al.*, 2022).

150

151 **3 Methods**

152 For this study, samples were taken at a ~30 cm resolution from slabbed core from 934–918 mbs for XRD and
153 mass spectrometry, as well as palynofacies and microcharcoal analysis. XRF analyses were made at a 1 cm
154 resolution from 934–918 mbs (complete dataset deposited as Damaschke *et al.*, 2021). These new samples
155 complement samples and data at 10 cm resolution from 951–934 mbs published in Hollaar *et al.* (2021).

156 **3.1 TOC, CaCO₃ and bulk organic carbon isotope mass spectrometry**

157 TOC and $\delta^{13}\text{C}_{\text{org}}$ were measured to track the changes in the total organic fraction and the bulk organic carbon
158 isotope ratios in relation to the other palaeoenvironmental proxy data.

159 Powdered bulk-rock samples (~ 2 g) were decarbonated in 50 ml of 3.3% HCl. After this, the samples were
160 transferred to a hot bath of 79 °C for 1 h to remove siderite and dolomite. Subsequently, the samples were
161 centrifuged and the liquid decanted. The samples were rinsed repeatedly with distilled water to reach neutral pH.
162 After this, the samples were oven-dried at 40 °C, re-powdered and weighed into tin capsules for mass
163 spectrometry using the Sercon Integra 2 stable isotope analyser at the University of Exeter Environment and
164 Sustainability Institute (ESI), stable isotope facility on the Penryn Campus, Cornwall. Samples were run
165 alongside in-house reference material (bovine liver; $\delta^{13}\text{C}$ -28.61 and Alanine; $\delta^{13}\text{C}$ -19.62) which was used to
166 correct for instrument drift and to determine the $\delta^{13}\text{C}$ values of the samples. The $\delta^{13}\text{C}_{\text{org}}$ values are reported

167 relative to V-PDB following a within-run laboratory standard calibration. Total organic carbon was determined
168 using the CO₂ beam area relative to the bovine liver standard (%C 47.24). Replicate analysis of the in-house
169 standards gave a precision of $\pm <0.1$ ‰ (2 SD).

170 The carbonate content was measured by the dry weight sample loss before and after decarbonation. The %C
171 content derived from the mass spectrometer was corrected for carbonate loss to derive TOC.

172 **3.2 X-Ray Diffraction (XRD) to determine clay mineralogy**

173 Clay mineral analysis was performed to gain insight into the relative importance of physical erosion versus
174 chemical weathering and related changes in the hydrological cycle.

175 About 2–3 g of gently powdered bulk-rock was decarbonated with a 0.2 M HCl solution. The clay sized fraction
176 (< 2 μm) was extracted with a syringe after decantation of the suspension after 95 minutes following Stokes'
177 law. The extracted fraction was centrifuged and oriented on glass slides for X-ray diffraction analysis (XRD)
178 using a Bruker D4 Endeavour diffractometer (Bruker, Billerica, MA, USA) with Cu K α radiations, LynxEye
179 detector and Ni filter under 40 kV voltage and 25 mA intensity (Biogéosciences Laboratory, Université
180 Bourgogne/Franche-Comté, Dijon). Following Moore and Reynolds (1997), the clay phases were discriminated
181 in three runs per sample: (1) air-drying at room temperature; (2) ethylene-glycol solvation for 24 h under
182 vacuum; (3) heating at 490 °C for 2 h.

183 Identification of the clay minerals was based on their main diffraction peaks and by comparison of the three
184 diffractograms obtained. The proportion of each clay mineral on glycolated diffractograms was measured using
185 the MACDIFF 4.2.5. software (Petschick, 2000). Identification of the clay minerals follows the methods in
186 Deconinck *et al.* (2019) and Moore and Reynolds (1997).

187 **3.3 Palynofacies and microcharcoal**

188 Palynofacies were examined to explore shifts in the terrestrial versus marine origins of the particulate organic
189 matter. Each ~ 20 g bulk rock sample was split into 0.5 cm³ fragments, minimizing breakage of charcoal and
190 other particles, to optimize the surface area for extraction of organic matter using a palynological acid
191 maceration technique. The samples were first treated with cold hydrochloric acid (10% and 37% HCl) to remove
192 carbonates. Following this, hydrofluoric acid (40% HF) was added to the samples to remove silicates. Carbonate
193 precipitation was prevented, by adding cold concentrated HCl (37%) after 48 h. The samples were neutralized
194 via multiple dilution-settling-decanting cycles using DI water, after which 5 droplets of the mixed residue were
195 taken for the analysis of palynofacies prior to sieving. The remaining residue was sieved through a 125 μm and
196 10 μm mesh to extract the microcharcoal fraction.

197 A known quantity (111 μl) out of a known volume of liquid containing the 10–125 μm sieved residue was
198 mounted onto a palynological slide using glycerine jelly. This fraction, containing the microscopic charcoal, was
199 analysed and the charcoal particles counted using an Olympus (BX53) transmitted light microscope (40 x10
200 magnification). For each palynological slide four transects (two transects in the middle and one on the left and
201 right side of the coverslip) were followed and the number of charcoal particles determined. Charcoal particles
202 were identified with the following criteria: opaque and black, often elongated lath-like shape with sharp edges,
203 original anatomy preserved, brittle appearance with a lustrous shine (Scott, 2010). These data were then scaled
204 up to the known quantity of the sample according the method of Belcher *et al.* (2005).

205 Palynofacies were grouped broadly according to Oboh-Ikuenobe *et al.* (2005): sporomorphs, fungal remains,
206 freshwater algae, marine palynomorphs, structured phytoclasts, unstructured phytoclasts, black debris,
207 amorphous organic matter (AOM), and charcoal (further described in Hollaar *et al.*, 2021). The palynofacies
208 were quantified on a palynological slide using the optical light microscope (40 x10 magnification) and counting
209 a minimum of 300 particles per slide. Because the samples are AOM-dominated, counting was continued until a
210 minimum of 100 non-AOM particles were observed. We used the percentage of terrestrial phytoclasts, which
211 includes sporomorphs, and structured and unstructured phytoclasts, to examine changes in terrestrial organic
212 particle content.

213

214 **3.4 X-Ray Fluorescence (XRF) to determine detrital elements**

215 Detrital elemental ratios were examined to analyse changes in relative terrestrial influx and the type of material
216 transported from the land to the marine realm. The slabbed archive halves of the Mochras borehole were
217 scanned via automated X-ray fluorescence (XRF) at a 1 cm resolution for the interval 951 –918 mbs, with the
218 ITRAX MC at the British Geological Survey Core Scanning Facility (CSF), Keyworth, UK (Damaschke *et al.*,
219 2021). The measurement window was 10 s and long-term drift in the measurement values was counteracted by
220 regular internal calibration with a glass reference (NIST-610). Duplicate measurements were taken every 5 m
221 for a 50 cm interval to additionally verify the measured results.

222 **3.5 Statistical analysis**

223 Principal component analysis (PCA) was performed to examine a potential change in the proxy data before and
224 after the +ve CIE. This was executed in the software PAST on the normalized dataset including microcharcoal,
225 TOC, CaCO₃, δ¹³C_{org}, S/I, K/I, primary clay mineralogy, Si/Al, Zr/Rb. The samples before the +ve CIE (951.0–
226 930.4 mbs) and the samples after the +ve CIE (930.3–918.0 mbs) are grouped to examine a potential difference
227 in the sedimentary composition before and after the +ve CIE. A Pearson's correlation was executed in Matlab
228 R2017b. The *p* value tests the hypothesis of no correlation against the alternative hypothesis of a positive or
229 negative correlation (significance level at $p \leq 0.05$).

230

231 **4 Results**

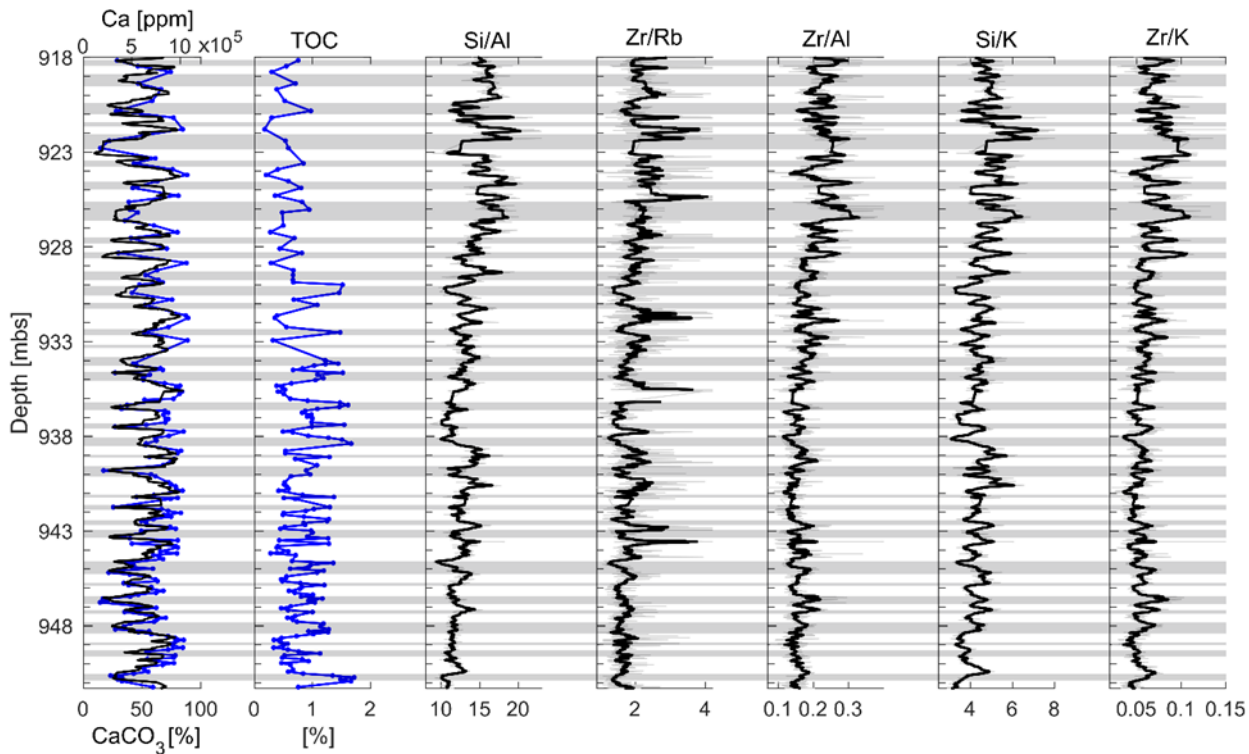
232

233 **4.1 TOC, CaCO₃ and bulk organic carbon isotope ratio mass spectrometry**

234 Alternating TOC-enhanced and Ca-rich lithological couplets occur on a metre scale through the studied interval
235 with TOC and CaCO₃ having a strong negative correlation ($r = -0.64$, $p = 0.001$). TOC content fluctuates in the
236 range 0.17–1.72 wt% (mean 0.8 wt%) and the highest fluctuations of TOC content are found from 939–930
237 mbs. The CaCO₃ content fluctuates in opposition to TOC and varies between 14 and 89 %. The studied interval
238 is generally high in CaCO₃ (mean 58 %) (Fig. 3). The δ¹³C_{org} displays a minor (~0.5 ‰) shift towards more
239 positive values at ~944 mbs (as reported in Storm *et al.*, 2020; Hollaar *et al.*, 2021). At ~ 930 mbs an abrupt
240 shift of ~1.8 ‰ (Figs. 1, 4; Storm *et al.*, 2020) indicates the onset of the Late Pliensbachian Event (LPE) in the
241 Mochras core. In agreement with this, the results of the present study show a shift from ~ minus 27 per mil to ~
242 minus 25.15 per mil between 930.8 and 930.4 mbs (Fig. 4). The δ¹³C_{org} data presented here have been divided
243 into three phases: the pre-LPE gradual rise, followed by the +ve CIE, which is subdivided into pulses 1, 2 and 3

244 (Fig. 1). After the onset of the positive $\delta^{13}\text{C}_{\text{org}}$ excursion, the TOC content drops to the lowest values (from 0.85
245 % before and 0.6 % after the +ve CIE on average), but the 1 metre fluctuations continue (Figs. 3, 4). No overall
246 change in the CaCO_3 content is observed through the positive carbon-isotope excursion (Fig. 3).

247



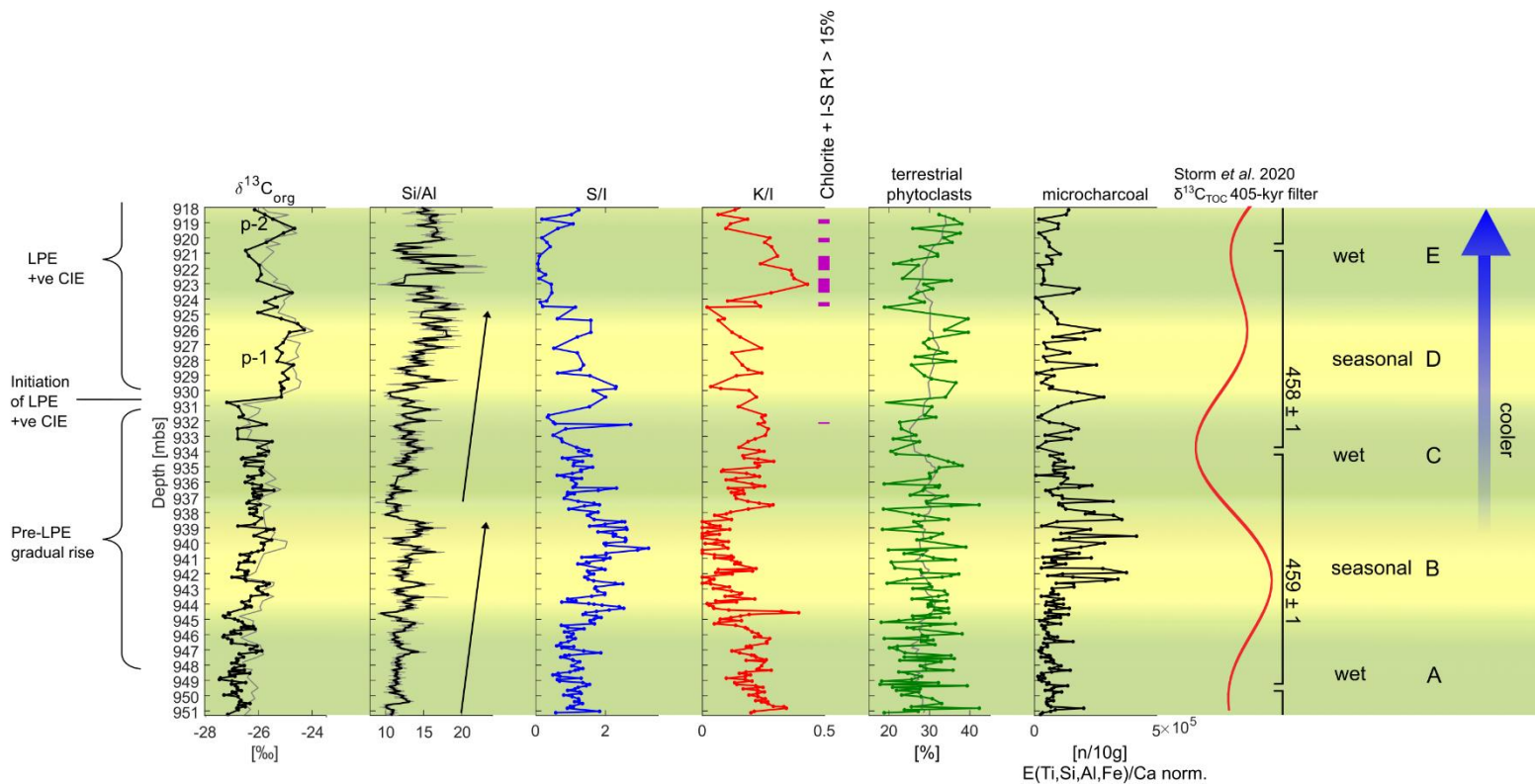
248

249 **Figure 3: Detrital ratios over the Ca-rich and TOC-enhanced lithological couplets for the studied**
250 **interval.** Overview of Ca (black, derived from Ruhl *et al.* 2016), CaCO_3 (blue), and TOC content of the studied
251 interval 951–918 mbs. The grey shading represents the TOC-enhanced beds and the unshaded bands mark the
252 Ca-rich (limestone) beds. The detrital ratios reflect the silt to fine sand fraction (Si, Zr) versus the clay fraction
253 (Rb, Al, K). Two increasing upward cycles are observed in the Si/Al and Zr/Rb ratios. The pattern observed in
254 all detrital ratios (except the Ti/Al) is similar and likely reflects overall upwards coarsening.

255

256 4.2 Clay minerals

257 XRD analysis shows that the main clay types found in this interval are illite, random illite-smectite mixed-layers
258 (I-S R0) [hereafter referred to as smectite], and kaolinite. Illite and kaolinite co-fluctuate in the interval studied
259 here, and are directly out of phase with smectite abundance. Chlorite and R1 I-S are present in minor
260 proportions, but reach sporadically higher relative abundance (> 10 %) from ~ 932 mbs upwards, with sustained
261 >10% abundance at ~925–918 mbs (Fig. 4 and SI Fig. 1). The relative abundances of smectite and illite and of
262 kaolinite and illite are expressed by the ratio S/I and K/I respectively. These ratios were calculated according to
263 the intensity of the main diffraction peak of each mineral.



265

266 **Figure 4: Synthesis diagram showing the climatic swings observed in tandem with the long eccentricity**
 267 **cycle.** The studied interval (Upper Pliensbachian Margaritatus Zone) comprises part of the pre-LPE gradual rise,
 268 the initiation of the LPE +ve CIE and pulse 1 and 2 ($\delta^{13}\text{C}_{\text{org}}$ data in black from this study and in light grey from
 269 Storm *et al.* (2020)). Five climatic phases (A–E) are interpreted from the Si/Al, smectite/illite, kaolinite/illite,
 270 chlorite and I-S R1 abundance and the microcharcoal abundance. In tandem with the 405 kyr cycle (Storm *et al.*,
 271 2020) climatic state of a year-round wet climate, low fire activity and fine-grained sediments across multiple
 272 precession cycles (phase A and C) alternates with a climatic state that includes repeated precessionally driven
 273 states that are semi-arid, with high fire activity and coarser sediments (phase B and D). The top of the record
 274 (phase E) indicates increased physical erosion (chlorite + I-S R1, kaolinite) relative to chemical weathering. In
 275 terrestrial phytoclast column grey line = 10-step moving average.

276

277

278 4.3 Organic matter

279 The type of particulate organic matter, and more specifically the abundance in the marine versus terrestrial
 280 origin of the particles, fluctuates on a metre scale from 18–42 % (Fig. 4, SI Fig. 2). Palynofacies indicate that
 281 the type of organic matter does not change in relation to the metre-scale lithological facies cycles (no correlation
 282 between percentage terrestrial phytoclasts and TOC or CaCO_3). No large and abrupt changes are recorded in the
 283 terrestrial/marine proportions, but the proportion of terrestrial phytoclasts has 4 high phases: between 944.6 and

284 942.0 mbs, 937.5 and 934.9 mbs, 930.4 and 925.4 mbs, and 920.3 and 918.0 mbs (SI Fig. 2). The first and
285 second high phase falls within the + 0.5 ‰ positive swing in the $\delta^{13}\text{C}_{\text{org}}$ whilst the latter two high phases
286 correspond to pulse 1 and pulse 2 in the +ve CIE. Amorphous organic matter (AOM) is very abundant, followed
287 by unstructured phytoclasts, with lower proportions of structured phytoclasts and charcoal (SI Fig. 3). Charcoal
288 particles make up a relatively large proportion of the terrestrial particulate organic matter (~10 % on average)
289 and ~3.5 % on average of the total particulate organic matter fraction (SI Fig. 3). Only sparse marine and
290 terrestrial palynomorphs were observed (SI Fig. 3).

291 To assess the character of the observed fluctuations in microcharcoal abundance, whether changes in
292 microcharcoal can be related to enhanced runoff from the land and/or organic preservation, or if the
293 microcharcoal signifies changes in fire activity on land, the charcoal record was corrected for detrital influx. We
294 adjust the charcoal particle abundances using the XRF elemental record, normalizing to the total terrigenous
295 influx following Daniau *et al.* (2013) and Hollaar *et al.* (2021). The stratigraphic trends in the normalized
296 microcharcoal for E_{ter}/Ca , Si/Al, Ti/Al and Fe/Al remain the same (SI Fig. 4). The absolute number of
297 microcharcoal particles decreases, with raw mean charcoal particles 1.06×10^5 per 10 g and E_{ter}/Ca normalized
298 mean 9.7×10^4 n/10g, Ti/Al normalized 6.4×10^4 n/10g, Si/Al normalized 7.7×10^4 n/10g, Fe/Al normalized
299 9.8×10^4 mean number of microcharcoal particles per 10 g (SI Fig. 4). The number of microcharcoal particles per
300 10 g processed rock decreases when correcting for terrestrial run-off changes, hinting that perhaps part of the
301 ‘background’ microcharcoal is related to terrestrial influx; the normalisation also shows that the observed
302 patterns in microcharcoal abundances are not influenced by changes in terrestrial runoff and taphonomy. Hence,
303 the highs and lows in the microcharcoal record can be interpreted to represent changes in the fire regime on
304 land. The microcharcoal abundance fluctuates strongly in the record presented here; however, no clear
305 difference in microcharcoal content has been observed before and after the onset of the +ve CIE.

306

307 **4.4 Detrital elemental ratios (XRF)**

308 Strong similarities are observed between the fluctuating ratios of Si/Al, Si/K, Zr/Rb, Zr/Al and Zr/K (Fig. 3).
309 The elements Al, Rb and K sit principally in the clay fraction (e.g. Calvert and Pederson, 2007), whereas Si and
310 Zr are often found in greater abundance in the coarser fraction related to silt and sand grade quartz and heavy
311 minerals (Calvert and Pederson, 2007). The ratios all show clear metre-scale fluctuations, and these are
312 superimposed on two increasing-upward trends observed in both the Si/Al and the Zr/Rb, followed by a drop
313 and rise to peak values in the latest part of phase D and phase E above the onset of the +ve CIE (Figs. 3, 4). A
314 parallel trend is observed between the clay ratios (XRD) and elemental ratios Si/Al and Zr/Rb (Fig. 3). Phases of
315 high S/I correspond to the peaks in the two coarsening upward sequences, whereas phases of high K/I
316 correspond to the low phases in the two coarsening upward sequences. After the +ve CIE onset (in phase E) this
317 relationship turns around, and an enrichment in the kaolinite/illite ratio corresponds to the elemental ratios,
318 where highest kaolinite relative abundance is observed in parallel with elemental ratios suggesting maximum
319 coarse fraction.

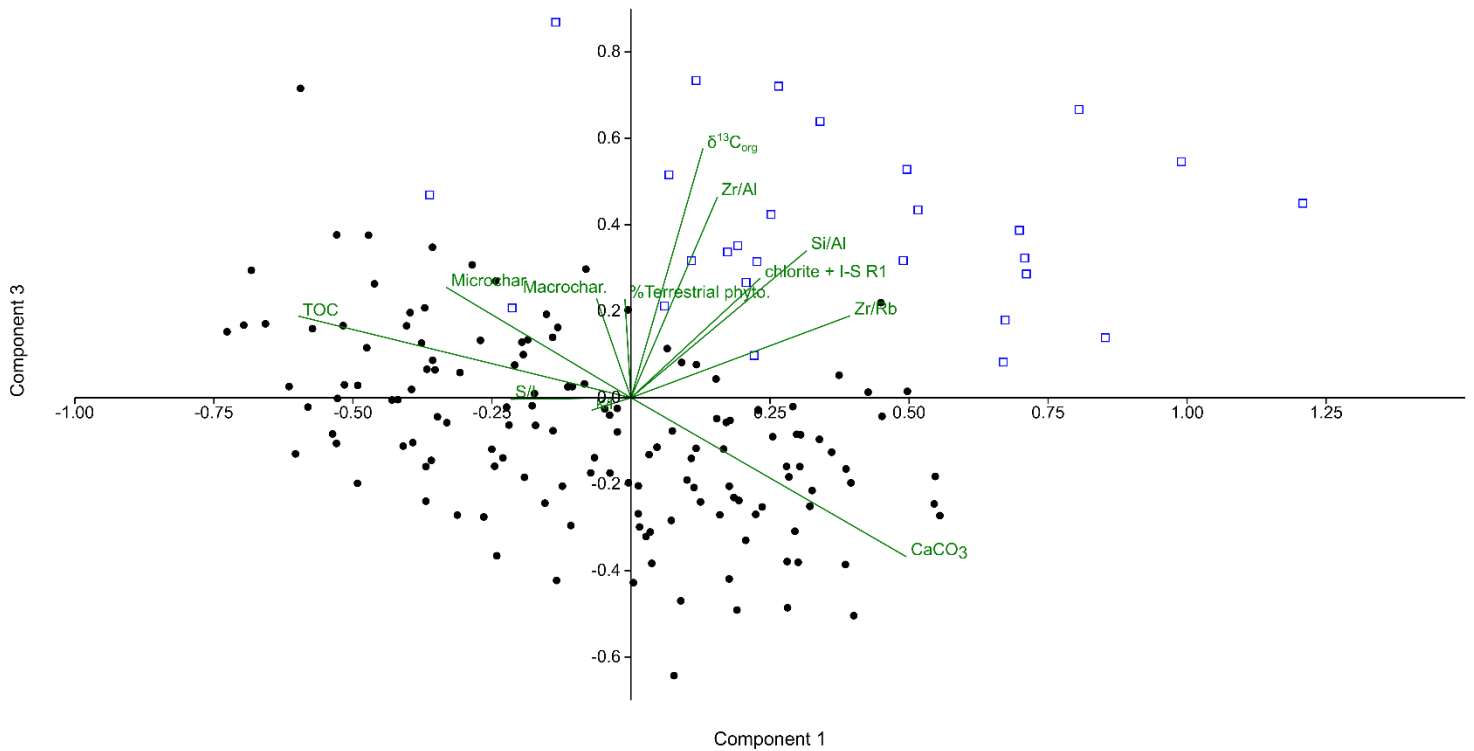
320

321 **4.5 PCA analysis**

322 The proxy datasets ($\delta^{13}\text{C}_{\text{org}}$, TOC, percentage terrestrial phytoclasts, microcharcoal, smectite/illite,
323 kaolinite/illite, abundance of chlorite and R1 I-S, Si/Al, Zr/Rb, Zr/Al) were normalized between 0–1 and run for
324 PCA analysis in PAST. Sixty-four percent of the variance is explained by the first three axes (PCA-1 27.7 %,
325 PCA-2 19.7 %, PCA-3 15.3 %) inside the 95 % confidence interval.

326 PC-1 mainly explains the anti-correlation of TOC and CaCO_3 . PC-2 shows the anti-correlation of K/I and S/I.
327 Positive loadings were observed for S/I, microcharcoal, macrocharcoal and CaCO_3 . For PC-2, negative loadings
328 were observed for K/I, abundance of chlorite + I-S R1. PC-3 shows strong positive loadings (> 0.3) for $\delta^{13}\text{C}_{\text{org}}$,
329 Si/Al and Zr/Al.

330 Plotting PC-1 (y-axis) over PC-3 (x-axis) shows that the samples after the onset of the +ve CIE are grouped to
331 the top of the y-axis (more associated with S/I compared to K/I) and to the right of the x-axis (more associated
332 with primary minerals, phytoclasts, and higher Si/Al, Zr/Rb and Zr/Al) (Fig. 5).



333 **Figure 5: PCA-analysis shows a distinctly different depositional signature before and after the onset of**
334 **the LPE +ve CIE in the Mochras core.** PCA plot of PC-1 and PC-3: all samples before the onset of the LPE
335 +ve CIE are marked in black closed circles and the samples after the onset of the LPE +ve CIE are marked in
336 blue open squares.

337

338 **5 Discussion**

339 Figure 1 provides the context for the LPE ‘cooling event’ at Mochras set within the background record. Shifts in
340 bulk $\delta^{18}\text{O}_{\text{carb}}$ are coeval to the $\delta^{13}\text{C}_{\text{org}}$ change to heavier isotopic values (~930 mbs) and reach a maximum in the
341 Margaritatus Zone (>1 ‰) (Ullmann *et al.*, 2022). The bulk oxygen-isotope excursions of Mochras are affected
342 by diagenesis and are deemed unlikely to reflect environmental conditions (Ullmann *et al.*, 2022). However,
343 oxygen isotope data from marine benthic and nektobenthic molluscs and brachiopods show heavier values
344 during the late Margaritatus Zone concurrent with a positive shift in $\delta^{13}\text{C}_{\text{org}}$, indicating cooling during the LPE
345 in the nearby Cleveland Basin (Robin Hood’s Bay and Staithes) (Korte and Hesselbo, 2011) and this trend is
346 also observed in several European sections (e.g. Korte *et al.*, 2015). The duration of the +ve CIE has been
347 estimated as ~0.4–0.6 Myr in the Cardigan Bay Basin (Ruhl *et al.*, 2016; Storm *et al.*, 2020; Pieńkowski *et al.*,
348 2021).

349

350 **5.1 Background sedimentological and environmental variations**

351 The Mochras succession shows metre-scale alternating TOC-enhanced and Ca-rich lithological couplets
352 (mudstone/limestone; Fig. 3). Previous assessments of the palaeoenvironmental signature of these TOC-
353 enhanced and Ca-rich couplets indicate strongly that the different depositional modes are driven by orbital
354 precession (Ruhl *et al.*, 2016; Hinnov *et al.*, 2018; Storm *et al.*, 2020; Hollaar *et al.*, 2021; Pieńkowski *et al.*,
355 2021). Precession driven changes in monsoonal strength have been suggested to influence the deposition and
356 preservation of TOC and carbonate in the Cardigan Bay Basin (Ruhl *et al.*, 2016), although the impact may have
357 been expressed, at least partially, by changes in strength of bottom currents in the seaway as a whole
358 (Pieńkowski *et al.*, 2021).

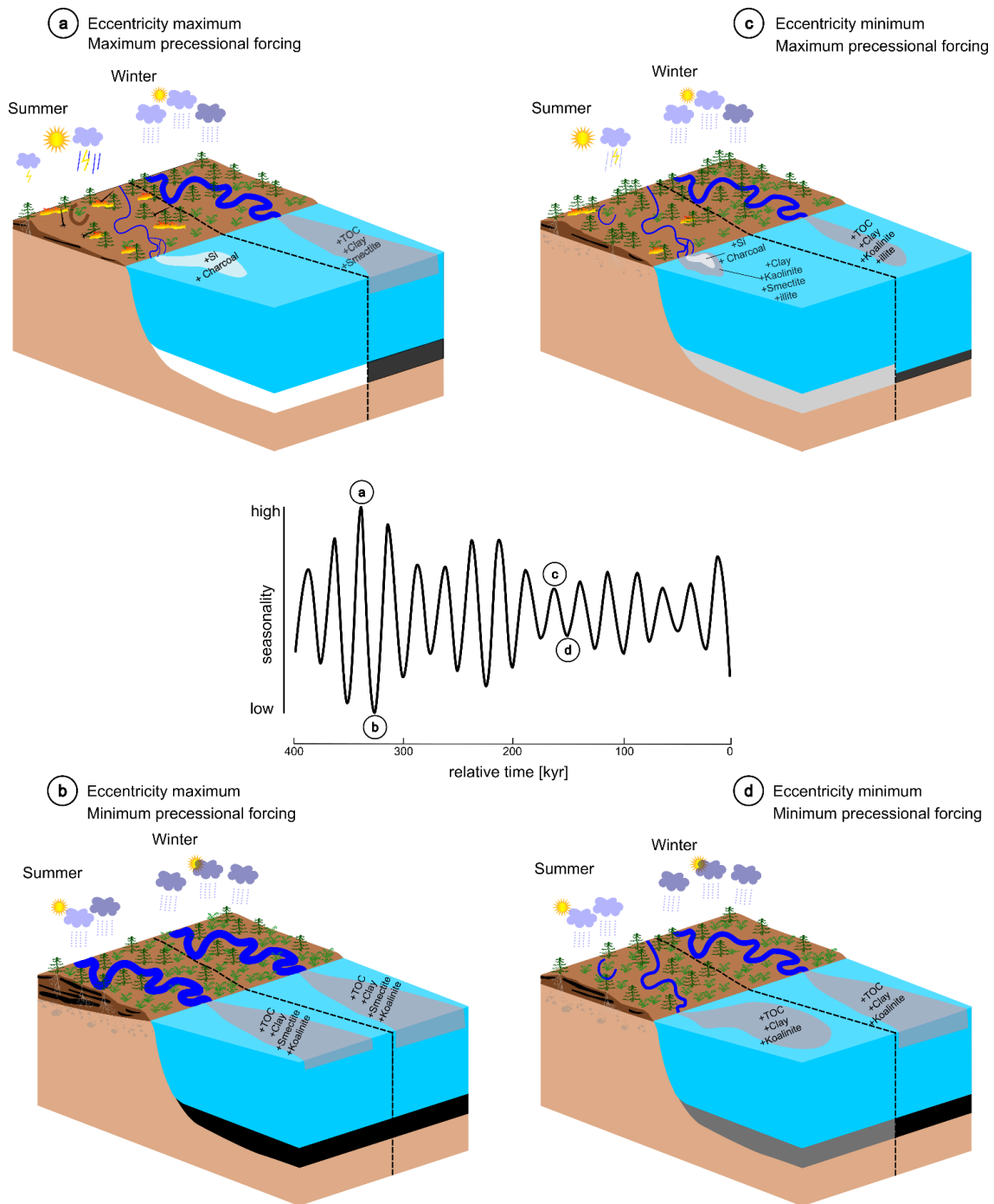
359 The preservation of primary carbonate is poor in the Mochras borehole, making it complex to determine in
360 detail the relative importance of carbonate producers for the bulk carbonate content (Ullmann *et al.*, 2022).
361 However, Early Jurassic, pelagic settings in the Tethys region often received abiotic fine-grained carbonate from
362 shallow marine carbonate platforms (Weedon, 1986; Cobianchi and Picotti, 2001; Krencker *et al.*, 2020) and
363 partly via carbonate producing organisms (such as coccolithophores in zooplankton pellets) (Weedon, 1986; van
364 de Schootbrugge *et al.*, 2005, e.g. Weedon *et al.*, 2019; Slater *et al.*, 2022). Coccolithophores are often poorly
365 preserved and recrystallized (Weedon, 1986; Weedon *et al.*, 2019; Slater *et al.*, 2022). The organic matter found
366 in the studied section of the Mochras borehole varies between 18 and 42% terrestrial phytoclasts (Fig. 4).
367 Phytoclasts are common, but palynomorphs are relatively sparse and poorly preserved. Marine amorphous
368 organic matter is the main constituent in the present study of particulate organic matter in unsieved macerated
369 samples, in the interval studied here (951–918 mbs). Examination of variations in the terrestrial/marine
370 proportions of organic matter, shows no correspondence between the type of organic matter and the TOC-
371 enhanced or Ca-rich lithological alternations. However, previous research has indicated that the percentage of
372 terrestrial phytoclasts show precession forcing independent of the lithological couplets (so out of phase with
373 precession scale changes in Ca-TOC content) between 951–934 mbs in the Mochras core (Hollaar *et al.*, 2021).
374 Such orbital forcing of the terrestrial vs marine proportions of organic matter were also found in Early Jurassic
375 sediments of Dorset, and were similarly independent of the lithological facies (Waterhouse, 1999). Terrestrial
376 phytoclast content show a weak expression of long-eccentricity driven variations in the section studied (Fig. 4).

377 Fossil charcoal makes up a substantial proportion of the organic fractions (11% of the terrestrial fraction) and
378 has previously been shown to vary considerably over long-eccentricity cycle 459 ± 1 peaking in abundance
379 during the phase of maximum eccentricity (Hollaar *et al.*, 2021). Microcharcoal also appears to be most
380 abundant during the maximum phase of the subsequent long eccentricity cycle 458 ± 1 (Fig. 4). Additionally,
381 K/I and S/I clay mineral ratios appear to alternate in response to long-eccentricity drivers (Fig. 4) up to 931 mbs
382 where the clay mineral signature changes. Detrital clays form in soil weathering profiles and/or physical
383 weathering of bedrock. Chemical weathering is enhanced in a high humidity environment with relatively high
384 temperatures and rainfall, when clays are formed in the first stages of soil development. In the modern day,
385 kaolinite is primarily formed in tropical soils, under year-round rainfall and high temperatures (Thiry, 2000).
386 Smectite also occurs in the tropics, but is more common in the subtropical to Mediterranean regions, where
387 humidity is still high, but periods of drought also occur (Thiry, 2000). Hence, smectite forms predominantly in
388 soil profiles under a warm and seasonally dry climate (Chamley, 1989; Raucsik and Varga, 2008), and kaolinite
389 in a year-round humid climate (Chamley, 1989; Ruffell *et al.*, 2002). Similarly, alternating intervals of kaolinite
390 and smectite dominance were observed for the Late Sinemurian (Munier *et al.*, 2021) and the Pliensbachian of
391 Mochras (Deconinck *et al.*, 2019).

392 The predominantly detrital character of these clay minerals has been confirmed by TEM scanning of
393 Pliensbachian smectite minerals, which revealed the fleecy morphology and lack of overgrowth (Deconinck *et*
394 *al.*, 2019). Therefore, the alternations of smectite and kaolinite are interpreted to reflect palaeoclimatic
395 signatures of a changing hydrological cycle, with a year-round wet climate evidenced by high K/I ratios, and a
396 more monsoon-like climate with seasonal rainfall with high S/I (Deconinck *et al.*, 2019; Hollaar *et al.*, 2021;
397 Munier *et al.*, 2021) (See Figs. 3, and 6). The intervals with a signal for weaker seasons appears to correspond to
398 phases of low eccentricity in the 405 kyr cycle, and signals of greater seasonality with periods of high more
399 pronounced eccentricity (Fig. 4) in the 405 kyr cycle. Between 951 and 930 mbs high K/I occurs during phases
400 of low long eccentricity suggesting an enhanced hydrological cycle (Hollaar *et al.*, 2021) with more intense
401 weathering, and enhanced fine grained terrestrial runoff to the marine record (Deconinck *et al.*, 2019). In
402 contrast, phases of maximum long-eccentricity appear to be smectite-rich, indicating seasonal rainfall, enhanced
403 fire (Hollaar *et al.*, 2021) and thus periods of droughts, and lower terrestrial runoff and subsequent lower
404 dilution (Deconinck *et al.*, 2019).

405 Detrital elemental ratios increase accordingly during the smectite-rich phases, and are lower during kaolinite-
406 rich phases between 951 and 930 mbs. Detrital elemental ratios can be used to explore changes in sediment
407 composition (e.g. Thibault *et al.*, 2018; Hesselbo *et al.*, 2020b) and the similarity of the long-term trend in Zr/Rb
408 and Si/Al (Fig. 3) indicates that these elemental ratios reflect grain size. The clay fraction (hosting Al, and Rb
409 (Chen *et al.*, 1999)), diminishes upwards, whereas the coarser silt to sand fraction (associated with Si (Hesselbo
410 *et al.*, 2020b) and Zr (Chen *et al.*, 2006)), increases upward (Figs. 3, 4). The grain size changes inferred here
411 reflect two overall coarsening upwards sequences (Figs. 3, 4). These sequences may reflect changes in clastic
412 transport due to changes in the proximity to the shore/siliciclastic source, changes in runoff due to a changing
413 hydrological cycle, changes in the intensity of weathering of the bedrock, or accelerated bottom currents with
414 greater carrying capacity of coarser sediments.

415



416

417

418 **Figure 6: Scheme of four environmental scenarios under the influence of eccentricity on a precessional**
 419 **time scale. (a) Most extreme seasonal contrast in the northern hemisphere occurs during maximum precessional**
 420 **forcing (i.e. low precession index) and maximum amplitude modulation by eccentricity. Seasonal contrast leads**
 421 **to a wet season that allows biomass to build up, high terrestrial runoff, and relatively enhanced organic burial in**
 422 **marine settings. During the dry season, fuel moisture levels are lower and fires are rapidly ignited and spread.**
 423 **Intensified monsoonal rains may lead to enhanced coarse-grained terrestrial runoff. Overall, less terrestrial**
 424 **runoff during this dry season results in less dilution of carbonate production, and/or less primary productivity of**

425 organic plankton. (b) Minimum precessional forcing and maximum amplitude modulation of eccentricity leads
426 to the least seasonal contrast. Chemical weathering on land is more intense during this year-round humid
427 climate. And although biomass is abundant, fire is suppressed due to the high moisture status. Both seasons are
428 humid and have considerable terrestrial runoff, resulting in marine organic burial. (c) Moderate seasonality
429 occurs during maximum precessional forcing and minimum amplitude modulation of the eccentricity cycle.
430 During the wet season biomass grows, and during the dry season fires can occur due to drier fuel conditions.
431 However, due to a lesser seasonal contrast the dry conditions are less pronounced and fire is not widespread.
432 Runoff includes coarse- and fine-grained sediments, and charcoal during the dry-season. (d) Seasonal contrast is
433 low during minimum precessional forcing and minimum amplitude modulation of the eccentricity cycle. Both
434 seasons were humid and experienced runoff of fine-grained sediments and organic burial in marine settings.
435 Moderately thick soil profiles could develop under this humid climate (figure developed from Martinez and
436 Dera, 2015).

437

438 **5.2 Depositional and environmental changes before and after the LPE +ve CIE**

439 **5.2.1 Climate forcing of the hydrological cycle**

440 The LPE +ve CIE begins around 930 mbs in the Mochras core and encompasses the remaining part of the
441 studied section (Fig. 4). We contrasted all the pre-CIE sediment signatures with those of the +ve CIE signatures
442 using principal components analysis which indicates distinctly different sedimentary composition and
443 environmental signature before and after the onset of the +ve CIE in Mochras (Fig. 5).

444 Before the +ve CIE onset, the clay mineral assemblage shows alternating phases of smectite and kaolinite,
445 indicating pedogenic weathering. The relative abundance of the detrital clay types observed in the studied
446 interval have the potential to hold important palaeoclimatic information regarding the hydrological cycle and the
447 relative proportion of chemical weathering and physical erosion. The hydrological cycle was forced by the 405
448 kyr eccentricity before the +CIE, with alternating eccentricity maxima linked to enhanced seasonality (smectite)
449 and eccentricity minima to an equitable wet climate (kaolinite) (Figs. 3, 6). and Higher frequency cycles are not
450 observed in the clay mineral ratios, with no precession or obliquity forcing detected in the high-resolution part
451 of the study 951–934 mbs (Hollaar *et al.*, 2021) and no expression of the 100 kyr cycle in the record presented
452 here. The formation of developed kaolinite-rich, and to a lesser extent smectite-rich soil profiles, requires a
453 steady landscape for many tens of thousands of years, although the ~1 Myr timescale of Thiry (2000) seems
454 excessive in our case given the clear expression of clay mineral changes through long-eccentricity cycles. Also,
455 the transportation and deposition of continental clays will occur after soil formation and add further time
456 between formation and final deposition (Chamley, 1989; Thiry, 2000). Thus, there is likely to be a lag of the
457 climatic signal observed in the marine sediments (Chamley, 1989; Thiry, 2000). However, we note that high
458 frequency climatic swings have been recorded in the clay mineral record in some instances, such as in the Lower
459 Cretaceous in SE Spain (Moiroud *et al.*, 2012). The limestone-marl alternations there are enhanced in smectite
460 versus kaolinite and illite, respectively, reflecting precession scale swings from a semi-arid to a tropical humid
461 climate (Moiroud *et al.*, 2012). Precession and higher frequency shifts in the clay record are likely caused by
462 fluctuations in runoff conditions rather than the formation of soils with a different clay fraction.

463 Directly after the initial +ve CIE shift from 930–924 mbs (Phase 1 of Fig. 4) little seems to change, and the
464 system evidently continued to respond as before to the long eccentricity forcing, despite the predicted cooling
465 (Korte and Hesselbo, 2011; Korte *et al.*, 2015; Gómez *et al.*, 2016). However, from around 924 mbs up to the
466 top of the studied section (Phase 2 of Fig. 4) the clay mineral assemblage displays a distinctly different
467 composition, with kaolinite dominating especially the early part of phase 2 of the LPE (Fig. 4). At the same time
468 there is an enhancement of the primary minerals illite and chlorite, and I-S R1 (Fig. 4 and SI Fig. 1). Although
469 an enhancement in detrital kaolinite indicates an acceleration of the hydrological cycle, detrital kaolinite is dual
470 in origin and can also be derived from reworking of the primary source material (Deconinck *et al.*, 2019). If the
471 climate is cooler, chemical weathering becomes less dominant and physical erosion of the bedrock becomes the
472 main detrital source of clay minerals. In the Cardigan Bay Basin, the bedrock of the surrounding Variscan
473 massifs (such as the Scottish, Welsh and Irish massifs) were a likely source of these clays. In the Early Jurassic
474 of the NW Tethys region, Lower Paleozoic mudrocks bearing mica-illite and chlorite were emergent (Merriman,
475 2006; Deconinck *et al.*, 2019), hence the enhancement of illite and chlorite likely indicates physical erosion in
476 the region surrounding the study site. Finally, authigenic clay particles could have been formed during burial
477 diagenesis. At temperatures between 60–70 °C smectite illitization occurs and I-S R1 is formed; however, the
478 high abundance of smectite in Mochras indicates limited burial diagenesis at that location (Deconinck *et al.*,
479 2019). Weak-moderate thermal diagenesis is confirmed for the Pliensbachian of Mochras, with T_{\max} from
480 pyrolysis analysis between 421 °C and 434 °C (van de Schootbrugge *et al.*, 2005; Storm *et al.*, 2020). Therefore,
481 I-S R1 in Mochras is interpreted to be derived from chemical weathering of illite (Deconinck *et al.*, 2019). The
482 coeval increase of these primary clay minerals, I-S R1 and kaolinite, indicate that during this period physical
483 erosion dominated over soil chemical weathering (Deconinck *et al.*, 2019; Munier *et al.*, 2021). This is similar
484 to what has been observed for the latest Pliensbachian in Mochras previously (Deconinck *et al.*, 2019).

485 Erosion of weathering profiles transports clay minerals (including kaolinite and smectite) to the marine realm. In
486 the ocean, the differential settling of kaolinite (near shore) and smectite (more distal) could occur based on the
487 morphology and size of clay particles (Thiry, 2000). However, comparison of long-term inferred regional sea
488 level changes from surrounding UK basins (Hesselbo, 2008) suggests that the relative proportions of smectite
489 and kaolinite are not influenced by changes in relative sea level in the Pliensbachian of Mochras (Deconinck *et al.*,
490 2019). On the assumption that the coarsening upward sequences at Mochras are indicative of relative sea
491 level change, it can also be argued that the proximity to shore did not impact the proportions of smectite and
492 kaolinite. Instead, we observe enhanced smectite during ‘proximal’ deposition and enhanced kaolinite at times
493 of more ‘distal’ deposition, the opposite of what might be expected (Fig. 4).

494 We suggest that the first phase of the LPE (Fig. 4, phase 1) was characterised by repeated periods of rainfall in a
495 seasonal climate forced by precession in which chemical weathering (smectite formation) dominated the
496 sedimentary signatures. This corresponds to maximum long-eccentricity and shows the same climatic signature
497 as during maximum eccentricity phases before the +ve CIE. This is then followed by a second phase (Fig. 4,
498 phase 2) where the climate is generally cooler, overall potentially more arid, but with rainfall throughout the
499 year over multiple precession cycles. This appears to have favoured deep physical erosion, owing to the
500 abundance of primary clay minerals, kaolinite and I-S R1. This interval corresponds to a minimum phase in the

501 405 kyr eccentricity based on Storm *et al.* (2020). This interpretation is further supported by decreasing and then
502 low microcharcoal abundance, pointing to suppression of fire activity at this time.

503

504 5.2.2 Climate forcing of sedimentary changes

505 Two coarsening upward cycles that predate the onset of the +ve CIE and continue for a few metres after its
506 initiation, are present in the detrital elemental ratios (best expressed in Si/Al and Zr/Rb records) (Figs. 3, 4), and
507 indicate a changing sediment influx over the studied interval. Previous study of the lithofacies of the Mochras
508 borehole has also shown the coarsening-upward sequences of 0.5–3 m thickness, which are observed to be
509 followed upwards by a thinner fining-upward succession (Pieńkowski *et al.*, 2021). This reported fining-upward
510 part is not reflected in the elemental ratios of the two sequences shown in this study. Furthermore, the coarsest
511 phases of these sequences are approximately coeval with decreasing trends in the K/I ratio and increasing trends
512 in the S/I. This could indicate that periods of a strong monsoonal/seasonal climate (indicated by S/I) brought
513 coarser grained material to the basin, whereas periods of year-round humidity (K/I) are associated with higher
514 chemical weathering (low Si/Al). Therefore, these two coarsening upwards cycles appear to link to increasing
515 long-eccentricity. A similar mechanism has been inferred for the northern South China Sea region in the
516 Miocene, where coarser grained material is found during periods of a strong summer monsoon and relatively
517 lower chemical weathering (Clift *et al.*, 2014). Present day studies show that bedrock erosion and associated
518 sediment transport is greater in areas with high seasonal contrast (Molnar, 2001; Molnar, 2004). Hence, the
519 Si/Al record also appears to reflect weathering and erosion conditions on land (Clift *et al.*, 2014, 2020), driven
520 by long-eccentricity modulated climate (SI Fig.5). However, other scenarios that would influence the grain size
521 on this time scale cannot be dismissed and include changes in proximity to siliciclastic source, or changes in
522 sediment transport via bottom water currents.

523 Changes in bottom water current strength and direction likely affected the depositional site of the Mochras core
524 (Pieńkowski *et al.*, 2021) although there is as yet no consensus on the processes that likely controlled these
525 palaeoceanographic parameters. In the UK region, the North Sea tectonic dome structure may have disrupted the
526 circulation in the N-S Laurasian Seaway (including the Viking Corridor) in the Late Pliensbachian when global
527 sea-levels are suggested to have been low (Haq 2018) and therefore diminished the connectivity between
528 western Tethys and the Boreal realm, hypothetically reducing poleward heat transport from the tropics (Korte *et al.*
529 *et al.*, 2015). This mechanism has also been argued to explain the later cooling observed in NW Europe during the
530 transition of the warmer Toarcian to the cooler Aalenian and Bajocian (Korte *et al.*, 2015). Late Pliensbachian
531 occlusion of the Viking Corridor is supported by the provincialism of marine faunas at this time, showing a
532 distinct Euro-Boreal province and a Mediterranean province (Dera *et al.*, 2011b). During the Toarcian, a
533 northward expansion of invertebrate faunal species has been found (Schweigert, 2005; Zakharov *et al.*, 2006;
534 Bourillot *et al.*, 2008; Nikitenko, 2008), indicating a northward (warmer) flow through the Viking corridor
535 (Korte *et al.*, 2015). More recently, a southward expansion of Arctic dinoflagellates into the Viking Corridor
536 was suggested for the termination of the T-OAE (van de Schootbrugge *et al.*, 2019), which is in agreement with
537 a N to S flow through the Viking Corridor suggested by numerical models (Bjerrum *et al.*, 2001; Dera and
538 Donnadieu, 2012; Ruvalcaba Baroni *et al.* 2018) and sparse Nd-isotopes (Dera *et al.*, 2009).

539 Over the European Epicontinental Shelf (EES), and the Tethys as a whole, a clockwise circular gyre likely
540 brought oxygenated warm Tethyan waters to the southwest shelf, with a progressively weaker north and
541 eastward flow due to rough bathymetry and substantial islands palaeogeography (Ruvalcaba Baroni *et al.*,
542 2018). This predominantly surface flow is modelled to have extended to shelfal sea floor depths. Only
543 episodically might nutrient-rich Boreal waters have penetrated south onto the EES in these coupled ocean-
544 atmosphere GCM model scenarios (Dera and Donnadieu, 2012). The modelling also suggests – counter-
545 intuitively – that the clockwise surface gyre of the Tethys extended further northwards and impacted the EES
546 more effectively when the Hispanic corridor was more open. The timing of the opening of the Hispanic corridor
547 is debated and varies from the Hettangian to Pliensbachian (Aberhan, 2001; Porter *et al.*, 2013; Sha, 2019).

548 An alternative bottom current configuration was discussed for Mochras specifically wherein changes in north-
549 to-south current strength (cf. Bjerrum *et al.*, 2001) are proposed for the changes in grain size and silt or sand
550 versus clay content via contour currents (Pieńkowski *et al.*, 2021). A strong flow from the cooler and shallow
551 boreal waters is hypothesized to have brought a coarser grainsize fraction in suspension and as bedload, which
552 was then deposited in the Cardigan Bay Basin while flowing to the deeper and warmer waters of the peri-Tethys
553 (Pieńkowski *et al.*, 2021). Times of a strong north to south current are proposed to be associated with more
554 oxygenated bottom waters (Pieńkowski *et al.*, 2021). In contrast, when the north to south current became
555 weaker, less coarse material will have been carried in suspension and as bedload, and a relatively higher clay
556 proportion will have been deposited in the Cardigan Bay Basin (Pieńkowski *et al.*, 2021). In this scenario, times
557 of sluggish currents are associated with low bottom water oxygenation (Pieńkowski *et al.*, 2021) and thus
558 climate forcing of current strength could explain the deposition of alternating coarser and finer fractions in the
559 Mochras borehole (Pieńkowski *et al.*, 2021).

560 Our research suggests that orbital cycles both before and during the onset of the +ve CIE have a significant
561 influence on seasonality and hydrology, affecting both fire regimes and sediment depositional character. Further
562 research is required to consider how long-eccentricity and obliquity cycles might interact with north-south flow
563 in the Cardigan Bay Basin and circulation processes. What is clear is that orbital cycles have impact on
564 terrestrial processes in the terrestrial sediment source areas (Hollaar *et al.*, 2021) and led to differences in
565 deposition within the marine sediments in the Mochras core (Ruhl *et al.*, 2016; Pieńkowski *et al.*, 2021). Our
566 data indicate that periods of coarser sediment deposition correspond to periods that include more seasonal
567 climates before the onset of the +ve CIE (low kaolinite), which is in line with the hypothesized grainsize
568 changes caused by contour currents (Pieńkowski *et al.*, 2021). However, after the onset of the +ve CIE, although
569 we suggest that the chemical weathering rate decreased, enhanced runoff and physical erosion are indicated by a
570 peak in primary clay minerals and K/I. Enhanced runoff could be expected to impact the thermohaline contour
571 currents (Dera and Donnadieu, 2012). Simultaneously, an increasingly cold climate (as indicated by enhanced
572 physical erosion over chemical weathering) indicates a boreal influence. It remains to be determined to what
573 extent orbital cycles might have the power to influence ocean circulation in the basin.

574 Relatively coarse sediments in the Late Pliensbachian have also been related to shallower sediment deposition in
575 UK basins (Hesselbo and Jenkyns, 1998; Hesselbo, 2008; Korte and Hesselbo, 2011). Around the UK area,
576 these regressive facies are plausibly related to enhanced sediment shedding from the North Sea dome structure
577 during sea level low stand across the region (Korte and Hesselbo, 2011). Sequence stratigraphy of the Lower

578 Jurassic of the Wessex, Cleveland and Hebrides basins (Hesselbo and Jenkyns, 1998; Hesselbo, 2008; Archer et
579 al., 2019) shows relative sea level changes and sand influxes in the late Margaritatus Zone in the studied basins.
580 Noteworthy in the Mochras borehole are phases of low $\delta^{18}\text{O}$ of macrofossils which seem to correspond to high
581 phases of macrofossil wood concomitant with low sea level, suggesting a possible control of relative sea level
582 on the oxygen-isotope record and the source of detrital material (Ullmann *et al.*, 2022). The broad spatial
583 distribution of these basins suggests that associated regression and/or sediment influx is of at least regional scale
584 (Hesselbo, 2008). The results presented here fall within this phase of regression (Hesselbo and Jenkyns,
585 1998; Hesselbo, 2008).

586 In the context of the North Sea topographic dome structure (occlusion of the Viking Corridor in regional ocean
587 flow) as a possible cause of the Late Pliensbachian cooling, these facies can be interpreted to represent
588 shallowing upward in relatively shallow water, or the supply of coarser sediment into a deep-water system. The
589 doming is hypothesized to have minimized or prohibited southward flow of cooler waters from the Boreal and
590 northward flow from warmer waters from the Mediterranean area (Korte *et al.*, 2015). The Mochras borehole is
591 situated on the southwestern flank of the dome and would have been cut-off from the northern parts of the
592 Laurasian Seaway, including the Hebrides Basin and Cleveland Basin (Korte *et al.*, 2015). This change in
593 seaway circulation could have impacted the source area of the detrital sediments in the Mochras borehole.

594 Superimposed on these larger-scale factors affecting grain size, orbital forcing clearly also had a strong impact.
595 The Cardigan Bay Basin (Mochras) is positioned about 290 km to the SW of the Cleveland Basin and at a
596 similar latitude, but to the W of the Wessex Basin (Ziegler, 1990; Torsvik and Cocks, 2017), and is therefore
597 expected to be impacted by the same regional changes in sea level and/or sediment flux. In the Late
598 Pliensbachian of the Cleveland Basin, the detrital ratios of Si/Al, Zr/Al and Zr/Rb show similar coarsening
599 upward sequences, which have been interpreted to reflect changes in riverine transport of siliciclastic grains and
600 grain size (Thibault *et al.*, 2018). The inferred changes in sea-level in the Cleveland Basin occur at a 100 kyr
601 pacing (Huang and Hesselbo, 2014; Hesselbo *et al.*, 2020b), potentially linking the regression cycles to short
602 eccentricity (Huang *et al.*, 2010 and refs therein) and long-eccentricity (Thibault *et al.*, 2018). This would mean
603 that eccentricity driven changes in inferred sea level change could be linked to glacioeustatic cycles during these
604 times (Brandt, 1986; Suan *et al.*, 2010; Korte and Hesselbo, 2011; Krencker *et al.*, 2019; Ruebsam *et al.*,
605 2019, 2020b; Ruebsam and Schwark, 2021; Ruebsam and Al-Husseini, 2021). Glacioeustatic sea level changes
606 are discussed for the Early Jurassic and Middle Jurassic (Krencker *et al.*, 2019; Bodin *et al.*, 2020; Ruebsam and
607 Schwark, 2021; Nordt *et al.*, 2022). A recent study on the rapid transgression observed at the Pliensbachian–
608 Toarcian boundary, ruled out other mechanisms that could force sea level at this time scale, such as aquifer-
609 eustasy, and emphasise that glacioeustatic changes in sea level are a likely possibility at times in the Early
610 Jurassic (Krencker *et al.*, 2019). Therefore, our findings overall are compatible with the episodic occurrence of
611 continental ice at the poles (Brandt, 1986; Price, 1999; Suan *et al.*, 2010; Korte and Hesselbo, 2011; Korte *et al.*,
612 2015; Bougeault *et al.*, 2017; Krencker *et al.*, 2019; Ruebsam *et al.*, 2019, 2020a, 2020b; Ruebsam and
613 Schwark, 2021; Ruebsam and Al-Husseini, 2021).

614

615 **6 Conclusions**

616 The terrestrial environment adjacent to the Cardigan Bay Basin was strongly influenced by orbitally driven
617 climate forcings (particularly precession and eccentricity) and colder climate linked to the Late Pliensbachian
618 Event (LPE). Long-eccentricity forcing remained strong both prior to and during the LPE. Our results identify
619 five swings in the climate in the study interval in tandem with the 405 kyr eccentricity minima and maxima.
620 Eccentricity maxima are linked to precessionally repeated occurrences of a semi-arid monsoonal climate with
621 high fire activity and relatively coarser sediment from terrestrial runoff. In contrast, 405 kyr minima in the
622 Mochras core are linked to a more persistent, annually wet climate, low fire activity, and relatively finer grained
623 deposits across multiple precession cycles. Although the 405 kyr cycle in the proxy records persists through the
624 onset of the LPE +ve CIE, the expression in the clay mineralogical record changes to indicate year-round
625 relatively cool and wet climate extended over multiple precession cycles driving significant erosion of bedrock.
626 Therefore, both the Milankovitch forcings and larger climatic shifts operate in tandem to govern changes in the
627 terrestrial environment.

628

629 **Data availability:** Supplementary data is available at the National Geoscience Data Centre at Keyworth
630 (NGDC) at (doi to be added) for the interval 934–918 mbs. All data presented for the interval 951–934 mbs is
631 available at the National Geoscience Data Centre at Keyworth (NGDC) at [https://doi.org/10.5285/d6b7c567-](https://doi.org/10.5285/d6b7c567-49f0-44c7-a94c-e82fa17ff98e)
632 [49f0-44c7-a94c-e82fa17ff98e](https://doi.org/10.5285/d6b7c567-49f0-44c7-a94c-e82fa17ff98e) (Hollaar *et al.*, 2021). The full Mochras XRF dataset is in Damaschke *et al.*
633 (2021).

634 **Author contribution:** CMB, SPH and TPH designed the research. TPH conducted the laboratory
635 measurements, with JFD contributing to the XRD-measurements and MD, CU and MJ to the XRF-
636 measurements. TPH, CMB and SPH wrote the manuscript, with contributions from all authors.

637 **Competing interests:** The authors declare that they have no conflict of interest.

638 **Acknowledgements:** This is a contribution to the JET project funded by the Natural Environment Research
639 Council (NERC) (grant number NE/N018508/1). SPH, CMB, JFD, CU, ML and TPH, acknowledge funding
640 from the International Continental Scientific Drilling Program (ICDP) and TPH acknowledges funding from the
641 University of Exeter. We thank the British Geological Survey (BGS), especially James Riding, Scott Renshaw
642 for facilitating access to the Mochras core. Also, Simon Wylde and Charles Gowing for their contribution to the
643 XRF scanning and discussion on the results. We further thank Chris Mitchell for help with the TOC and $\delta^{13}\text{C}_{\text{org}}$
644 analyses. Finally, we thank Ludovic Bruneau for technical assistance with the XRD-analysis. We thank referees
645 Stéphane Bodin and Wolfgang Ruebsam for their very helpful comments and Mathieu Martinez for informal
646 discussion.

647

648 **References**

649 Aberhan, M. Bivalve palaeobiogeography and the Hispanic Corridor: time of opening and effectiveness of a
650 proto-Atlantic seaway, *Palaeogeogr. Palaeoclimatol.*, 165(3-4), 375 – 394, [https://doi.org/10.1016/S0031-](https://doi.org/10.1016/S0031-0182(00)00172-3)
651 [0182\(00\)00172-3](https://doi.org/10.1016/S0031-0182(00)00172-3), 2001.

652 Alberti, M., Fürsich, F. T., and Andersen, N.: First steps in reconstructing Early Jurassic sea water temperatures
653 in the Andean Basin of northern Chile based on stable isotope analyses of oyster and brachiopod shells, *J.*
654 *Palaeogeogr.*, 8(1), 1 – 17, <https://doi.org/10.1186/s42501-019-0048-0>, 2019.

655 Alberti, M., Parent, H., Garrido, A.C., Andersen, N., Garbe-Schönberg, D., and Danise, S.: Stable isotopes
656 ($\delta^{13}\text{C}$, $\delta^{18}\text{O}$) and element ratios (Mg/Ca, Sr/Ca) of Jurassic belemnites, bivalves and brachiopods from the
657 Neuquén Basin (Argentina): challenges and opportunities for palaeoenvironmental reconstructions, *J. Geol.*
658 *Soc.*, 178(1), <https://doi.org/10.1144/jgs2020-16>, 2021.

659 Archer, S.G., Steel, R.J., Mellere, D., Blackwood, S., and Cullen, B.: Response of Middle Jurassic shallow-
660 marine environments to syn-depositional block tilting: Isles of Skye and Raasay, NW Scotland, *Scot. J. Geol.*,
661 55(1), 35 – 68, <https://doi.org/10.1144/sjg2018-014>, 2019.

662 Bailey, T.R., Rosenthal, Y., McArthur, J.M., Van de Schootbrugge, B., and Thirlwall, M.F.: Paleoceanographic
663 changes of the Late Pliensbachian–Early Toarcian interval: a possible link to the genesis of an Oceanic Anoxic
664 Event, *Earth Planet. Sc. Lett.*, 212(3 – 4), 307 – 320, [https://doi.org/10.1016/S0012-821X\(03\)00278-4](https://doi.org/10.1016/S0012-821X(03)00278-4), 2003.

665 Beckmann, B., Flögel, S., Hofmann, P., Schulz, M., and Wagner, T.: Upper Cretaceous African climate
666 development and implications for the marine carbon cycle, *Nature*, 437, 241 – 244,
667 <https://doi.org/10.1038/nature03976>, 2005.

668 Belcher, C.M., Collinson, M.E., and Scott, A.C.: Constraints on the thermal energy released from the Chicxulub
669 impactor: new evidence from multi-method charcoal analysis, *J. Geol. Soc.*, 162(4), 591 – 602,
670 <https://doi.org/10.1144/0016-764904-104>, 2005.

671 Bjerrum, C. J., Surlyk, F., Callomon, J.H., and Slingerland, R.L.: Numerical paleoceanographic study of the
672 Early Jurassic transcontinental Laurasian Seaway, *Paleoceanography*, 16(4), 390 – 404,
673 <https://doi.org/10.1029/2000PA000512>, 2001.

674 Bodin, S., Fantasia, A., Krencker, F.N., Nebsbjerg, B., Christiansen, L., and Andrieu, S.: More gaps than record!
675 A new look at the Pliensbachian/Toarcian boundary event guided by coupled chemo-sequence stratigraphy.
676 *Palaeogeogr. Palaeocl.*, 610, 111344, <https://doi.org/10.1016/j.palaeo.2022.111344>, 2023.

677 Bodin, S., Mau, M., Sadki, D., Danisch, J., Nutz, A., Krencker, F.N., and Kabiri, L.: Transient and secular
678 changes in global carbon cycling during the early Bajocian event: Evidence for Jurassic cool climate episodes,
679 *Global Planet. Change*, 194, 103287, <https://doi.org/10.1016/j.gloplacha.2020.103287>, 2020.

680 Bougeault, C., Pellenard, P., Deconinck, J.F., Hesselbo, S.P., Dommergues, J.L., Bruneau, L., Cocquerez, T.,
681 Laffont, R., Huret, E. and Thibault, N.: Climatic and palaeoceanographic changes during the Pliensbachian
682 (Early Jurassic) inferred from clay mineralogy and stable isotope (CO) geochemistry (NW Europe), *Global*
683 *Planet. Change*, 149, <https://doi.org/10.1016/j.gloplacha.2017.01.005>, 2017.

684 Bourillot, R., Neige, P., Pierre, A., and Durllet, C.: Early–middle Jurassic Lytoceratid ammonites with
685 constrictions from Morocco: palaeobiogeographical and evolutionary implications, *Palaeontology*, 51(3), 597 –
686 609, <https://doi.org/10.1111/j.1475-4983.2008.00766.x>, 2008.

- 687 Brandt, K.: Glacioeustatic cycles in the Early Jurassic?, *Neues Jahrbuch für Geologie und Paläontologie-*
688 *Monatshefte*, 257 – 274, <https://doi.org/10.1127/njgpm/1986/1986/257>, 1986.
- 689 Calvert, S.E., and Pedersen, T.F.: Chapter fourteen elemental proxies for palaeoclimatic and palaeoceanographic
690 variability in marine sediments: interpretation and application, *Dev. Mar. Geol.*, 1, 567 – 644,
691 [https://doi.org/10.1016/S1572-5480\(07\)01019-6](https://doi.org/10.1016/S1572-5480(07)01019-6), 2007.
- 692 Chamley, H.: *Clay Sedimentology*, Springer Verlag, Berlin, 623 pp., ISBN 978-3-642-85918-8, 1989.
- 693 Chen, J., An, Z., and Head, J.: Variation of Rb/Sr ratios in the loess-paleosol sequences of central China during
694 the last 130,000 years and their implications for monsoon paleoclimatology, *Quat. Res.*, 51(3), 215 – 219,
695 <https://doi.org/10.1006/qres.1999.2038>, 1999.
- 696 Chen, J., Chen, Y., Liu, L., Ji, J., Balsam, W., Sun, Y., and Lu, H.: Zr/Rb ratio in the Chinese loess sequences
697 and its implication for changes in the East Asian winter monsoon strength, *Geochim. Cosmochim. Acta*, 70(6),
698 1471 – 1482, <https://doi.org/10.1016/j.gca.2005.11.029>, 2006.
- 699 Cifer, T., Goričan, Š., Auer, M., Demény, A., Fraguas, Á., Gawlick, H J., and Riechelmann, S.: Integrated
700 stratigraphy (radiolarians, calcareous nannofossils, carbon and strontium isotopes) of the Sinemurian–
701 Pliensbachian transition at Mt. Rettenstein, Northern Calcareous Alps, Austria, *Global Planet. Change*, 212,
702 103811, <https://doi.org/10.1016/j.gloplacha.2022.103811>, 2022.
- 703 Clift, P.D., Kulhanek, D.K., Zhou, P., Bowen, M.G., Vincent, S.M., Lyle, M., and Hahn, A.: Chemical
704 weathering and erosion responses to changing monsoon climate in the Late Miocene of Southwest Asia, *Geol.*
705 *Mag.*, 157(6), 939 – 955, <https://doi.org/10.1017/S0016756819000608>, 2020.
- 706 Clift, P.D., Wan, S., and Blusztajn, J.: Reconstructing chemical weathering, physical erosion and monsoon
707 intensity since 25 Ma in the northern South China Sea: a review of competing proxies, *Earth Sci. Rev.*, 130, 86
708 – 102, <https://doi.org/10.1016/j.earscirev.2014.01.002>, 2014.
- 709 Copestake, P., and Johnson, B.: Lower Jurassic Foraminifera from the Llanbedr (Mochras Farm) Borehole,
710 North Wales, UK, *Monographs of the Palaeontographical Society*, 167(641), 1 – 403, 2014.
- 711 Damaschke, M., Wylde, S., Jiang, M., Hollaar, T., Ullmann, C.V.: Llanbedr (Mochras Farm) Core Scanning
712 Dataset. NERC EDS National Geoscience Data Centre. (Dataset). [https://doi.org/10.5285/c09e9908-6a21-43a8-](https://doi.org/10.5285/c09e9908-6a21-43a8-bc5a-944f9eb8b97e)
713 [bc5a-944f9eb8b97e](https://doi.org/10.5285/c09e9908-6a21-43a8-bc5a-944f9eb8b97e), 2021.
- 714 Damborenea, S. E., Echevarria, J., and Ros-Franch, S.: Southern Hemisphere Palaeobiogeography of Triassic-
715 Jurassic Marine Bivalves, *Springer Briefs Seaways and Landbridges: Southern Hemisphere Biogeographic*
716 *Connections Through Time*, Springer Science and Business Media, Berlin, [https://doi.org/10.1007/978-94-007-](https://doi.org/10.1007/978-94-007-5098-2_1)
717 [5098-2_1](https://doi.org/10.1007/978-94-007-5098-2_1), 2013.
- 718 Daniau, A.L., Sánchez Goñi, M.F., Martinez, P., Urrego, D.H., Bout-Roumazelles, V., Desprat, S., and Marlon,
719 J.R.: Orbital-scale climate forcing of grassland burning in southern Africa, *Proceedings of the National*
720 *Academy of Sciences*, 110(13), 5069-5073, <https://doi.org/10.1073/pnas.1214292110>, 2013.

721 Deconinck, J.F., Hesselbo, S.P., and Pellenard, P.: Climatic and sea-level control of Jurassic (Pliensbachian)
722 clay mineral sedimentation in the Cardigan Bay Basin, Llanbedr (Mochras Farm) borehole, Wales,
723 *Sedimentology*, 66, 2769–2783, <https://doi.org/10.1111/sed.12610>, 2019.

724 Dera, G., and Donnadieu, Y.: Modeling evidences for global warming, Arctic seawater freshening, and sluggish
725 oceanic circulation during the Early Toarcian anoxic event, *Paleoceanography*, 27(2),
726 <https://doi.org/10.1029/2012PA002283>, 2012.

727 Dera, G., Neige, P., Dommergues, J.L., and Brayard, A.: Ammonite paleobiogeography during the
728 Pliensbachian–Toarcian crisis (Early Jurassic) reflecting paleoclimate, eustasy, and extinctions, *Global Planet.*
729 *Change*, 78(3–4), 92–105, <https://doi.org/10.1016/j.gloplacha.2011.05.009>, 2011.

730 Dera, G., Pucéat, E., Pellenard, P., Neige, P., Delsate, D., Joachimski, M.M., Reisberg, L., and Martinez, M.:
731 Water mass exchange and variations in seawater temperature in the NW Tethys during the Early Jurassic:
732 evidence from neodymium and oxygen isotopes of fish teeth and belemnites, *Earth Planet. Sc. Lett.*, 286, 198–
733 207, <https://doi.org/10.1016/j.epsl.2009.06.027>, 2009.

734 de Graciansky, P.C., Jacquin, T., and Hesselbo, S.P. (Eds.): The Ligurian cycle: An overview of Lower Jurassic
735 2nd-order transgressive-regressive facies cycles in western Europe, *Mesozoic and Cenozoic Sequence*
736 *Stratigraphy of European Basins*, SEPM special publication, 60, 467–479, ISBN 1-565776-043-3, 1998.

737 De Lena, L.F., Taylor, D., Guex, J., Bartolini, A., Adatte, T., van Acken, D., Spangenberg, J.E., Samankassou,
738 E., Vennemann, T. and Schaltegger, U.: The driving mechanisms of the carbon cycle perturbations in the late
739 Pliensbachian (Early Jurassic), *Sci. Rep-UK*, 9(1), 1–12, <https://doi.org/10.1038/s41598-019-54593-1>, 2019.

740 Dobson, M.R. and Whittington, R.J.: The geology of Cardigan Bay, *P. Geologist. Assoc.*, 98, 331–353,
741 [https://doi.org/10.1016/S0016-7878\(87\)80074-3](https://doi.org/10.1016/S0016-7878(87)80074-3), 1987.

742 Franceschi, M., Dal Corso, J., Posenato, R., Roghi, G., Masetti, D., and Jenkyns, H.C.: Early Pliensbachian
743 (Early Jurassic) C-isotope perturbation and the diffusion of the Lithiotis Fauna: insights from the western
744 Tethys, *Palaeogeogr. Palaeocl.*, 410, 255–263, <https://doi.org/10.1016/j.palaeo.2014.05.025>, 2014.

745 Gómez, J.J., Comas-Rengifo, M.J., and Goy, A.: Palaeoclimatic oscillations in the Pliensbachian (Early
746 Jurassic) of the Asturian Basin (Northern Spain), *Clim. Past*, 12(5), 1199–1214, [https://doi.org/10.5194/cp-12-](https://doi.org/10.5194/cp-12-1199-2016)
747 [1199-2016](https://doi.org/10.5194/cp-12-1199-2016), 2016.

748 Hallam, A.: A revised sea-level curve for the early Jurassic, *J. Geol. Soc.*, 138(6), 735–743,
749 <https://doi.org/10.1144/gsjgs.138.6.0735>, 1981.

750 Haq, B.U.: Jurassic sea-level variations: a reappraisal, *GSA today*, 28(1), 4–10, 2018.

751 Hesselbo, S.P., Bjerrum, C.J., Hinnov, L.A., MacNiocaill, C., Miller, K.G., Riding, J.B., van de Schootbrugge,
752 B., and the Mochras Revisited Science Team: Mochras borehole revisited: a new global standard for Early
753 Jurassic earth history, *Sci. Dril.*, 16, 81–91, <https://doi.org/10.5194/sd-16-81-2013>, 2013.

- 754 Hesselbo, S.P., and Jenkyns, H.C. (Eds.): British Lower Jurassic sequence stratigraphy, Mesozoic and Cenozoic
755 Sequence Stratigraphy of European Basins, SEPM special publication, 60, 561 – 581, ISBN 1-565776-043-3,
756 1998.
- 757 Hesselbo, S.P.: Sequence stratigraphy and inferred relative sea-level change from the onshore British Jurassic,
758 P. Geologist. Assoc., 119, 19–34, [https://doi.org/10.1016/S0016-7878\(59\)80069-9](https://doi.org/10.1016/S0016-7878(59)80069-9), 2008.
- 759 Hesselbo, S.P., Ogg, J.G., Ruhl, M., Hinnov, L.A., and Huang, C.J.: The Jurassic Period, in: Geological Time
760 Scale 2020, edited by: Gradstein, F.M., Ogg, J.G., Schmitz, M.D., and Ogg, G.M. (Eds.), Elsevier, 955 – 1021,
761 2020a.
- 762 Hesselbo, S.P., Hudson, A.J. L., Huggett, J.M., Leng, M.J., Riding, J.B., and Ullmann, C.V.: Palynological,
763 geochemical, and mineralogical characteristics of the Early Jurassic Liasidium Event in the Cleveland Basin,
764 Yorkshire, UK, Newsl. Stratigr., 53, 191–211, <https://doi.org/10.1127/nos/2019/0536>, 2020b.
- 765 Hinnov, L.A., Ruhl, M., and Hesselbo, S.P.: Reply to the Comment on “Astronomical constraints on the
766 duration of the Early Jurassic Pliensbachian Stage and global climatic fluctuations” [Earth Planet. Sci. Lett. 455
767 (2016) 149 – 165], Earth Planet. Sc. Lett., 481, 415 – 419, <https://doi.org/10.1016/j.epsl.2016.08.038>, 2018.
- 768 Hollaar, T.P., Baker, S.J., Hesselbo, S.P., Deconinck, J.F., Mander, L., Ruhl, M., and Belcher, C.M.: Wildfire
769 activity enhanced during phases of maximum orbital eccentricity and precessional forcing in the Early Jurassic,
770 Commun. Earth Environ., 2(1), 1 – 12, <https://doi.org/10.1038/s43247-021-00307-3>, 2021.
- 771 Huang, C., and Hesselbo, S.P.: Pacing of the Toarcian Oceanic Anoxic Event (Early Jurassic) from astronomical
772 correlation of marine sections, Gondwana Res., 25(4), 1348 – 1356, <https://doi.org/10.1016/j.gr.2013.06.023>,
773 2014.
- 774 Huang, C., Hesselbo, S.P., and Hinnov, L.: Astrochronology of the late Jurassic Kimmeridge Clay (Dorset,
775 England) and implications for Earth system processes, Earth Planet. Sc. Lett., 289(1 – 2), 242 – 255,
776 <https://doi.org/10.1016/j.epsl.2009.11.013>, 2010.
- 777 Ilyina, V.I.: Jurassic palynology of Siberia, Hayka, 1985.
- 778 Ivimey-Cook, H.C.: Stratigraphical palaeontology of the Lower Jurassic of the Llanbedr (Mochras Farm)
779 Borehole, in: The Llandbedr (Mochras Farm) Borehole, edited by: Woodland, A.W., 87 – 92, (Rep. No. 71/18,
780 Institute of Geological Sciences, 1971), 1971.
- 781 Jenkyns, H.C., and Clayton, C.J.: Black shales and carbon isotopes in pelagic sediments from the Tethyan
782 Lower Jurassic, Sedimentology, 33(1), 87 – 106, <https://doi.org/10.1111/j.1365-3091.1986.tb00746.x>, 1986.
- 783 Kaplan, M.E.: Calcite pseudomorphoses in Jurassic and Lower Cretaceous deposits of the northern area of
784 eastern Siberia, Geologiya i Geofizika, 19, 62 – 70, 1978.
- 785 Korte, C., Hesselbo, S.P., Ullmann, C.V., Dietl, G., Ruhl, M., Schweigert, G., and Thibault, N.: Jurassic climate
786 mode governed by ocean gateway, Nat Commun, 6(1), 1 – 7, <https://doi.org/10.1038/ncomms10015>, 2015.

787 Korte, C. and Hesselbo, S. P.: Shallow-marine carbon- and oxygen-isotope and elemental records indicate
788 icehouse-greenhouse cycles during the Early Jurassic, *Paleoceanography*, 26, PA4219,
789 <https://doi.org/10.1029/2011PA002160>, 2011.

790 Krencker, F.N., Fantasia, A., Danisch, J., Martindale, R., Kabiri, L., El Ouali, M., and Bodin, S.: Two-phased
791 collapse of the shallow-water carbonate factory during the late Pliensbachian–Toarcian driven by changing
792 climate and enhanced continental weathering in the Northwestern Gondwana Margin, *Earth-Sci. Rev.*, 208,
793 103254, <https://doi.org/10.1016/j.earscirev.2020.103254>, 2020.

794 Krencker, F.N., Lindström, S., and Bodin, S.: A major sea-level drop briefly precedes the Toarcian oceanic
795 anoxic event: implication for Early Jurassic climate and carbon cycle, *Sci Rep-UK*, 9(1), 1 – 12,
796 <https://doi.org/10.1038/s41598-019-48956-x>, 2019.

797 Laskar, J., Fienga, A., Gastineau, M., and Manche, H.: La2010: a new orbital solution for the long-term motion
798 of the Earth, *Astron Astrophys*, 532, A89, <https://doi.org/10.1051/0004-6361/201116836>, 2011.

799 Laskar, J.: Astrochronology, in: *Geological Time Scale*, edited by: Gradstein, F.M., Ogg, J.G., and Ogg, G.M.,
800 Elsevier, 139 – 158, <https://doi.org/10.1016/B978-0-12-824360-2.00004-8>, 2020.

801 Martinez, M., and Dera, G.: Orbital pacing of carbon fluxes by a~ 9-My eccentricity cycle during the Mesozoic,
802 *P. Natl. Acad. Sci. USA*, 112(41), 12604-12609, <https://doi.org/10.1073/pnas.1419946112>, 2015.

803 McArthur, J.M., Donovan, D.T., Thirlwall, M.F., Fouke, B.W., and Matthey, D.: Strontium isotope profile of the
804 early Toarcian (Jurassic) oceanic anoxic event, the duration of ammonite biozones, and belemnite
805 palaeotemperatures, *Earth Planet. Sc. Lett.*, 179(2), 269 – 285, [https://doi.org/10.1016/S0012-821X\(00\)00111-4](https://doi.org/10.1016/S0012-821X(00)00111-4),
806 2000.

807 McElwain, J.C., Wade-Murphy, J., and Hesselbo, S.P.: Changes in carbon dioxide during an oceanic anoxic
808 event linked to intrusion into Gondwana coals, *Nature*, 435(7041), 479 – 482,
809 <https://doi.org/10.1038/nature03618>, 2005.

810 Mercuzot, M., Pellenard, P., Durllet, C., Bougeault, C., Meister, C., Dommergues, J.L., Thibault, N., Baudin, F.,
811 Mathieu, O., Bruneau, L., Huret, E., and El Hmidi, K.: Carbon-isotope events during the Pliensbachian (Lower
812 Jurassic) on the African and European margins of the NW Tethyan Realm, *Newsl. Stratigr.*, 41 – 69,
813 <https://doi.org/10.1127/nos/2019/0502>, 2020.

814 Merriman, R.J.: Clay mineral assemblages in British Lower Palaeozoic mudrocks, *Clay Miner.*, 41, 473–512,
815 <https://doi.org/10.1180/0009855064110204>, 2006.

816 Moiroud, M., Martinez, M., Deconinck, J.F., Monna, F., Pellenard, P., Riquier, L., and Company, M.: High-
817 resolution clay mineralogy as a proxy for orbital tuning: example of the Hauterivian–Barremian transition in the
818 Betic Cordillera (SE Spain), *Sediment. Geol.*, 282, 336 – 346, <https://doi.org/10.1016/j.sedgeo.2012.10.004>,
819 2012.

820 Molnar, P.: Climate change, flooding in arid environments, and erosion rates, *Geology*, 29(12), 1071 – 1074,
821 [https://doi.org/10.1130/0091-7613\(2001\)029<1071:CCFIAE>2.0.CO;2](https://doi.org/10.1130/0091-7613(2001)029<1071:CCFIAE>2.0.CO;2), 2001.

- 822 Molnar, P.: Late Cenozoic increase in accumulation rates of terrestrial sediment: How might climate change
823 have affected erosion rates?, *Annu. Rev. Earth Pl. Sc.*, 32, 67 – 89,
824 <https://doi.org/10.1146/annurev.earth.32.091003.143456>, 2004.
- 825 Moore, D.M. and Reynolds, R.C.: *X-Ray Diffraction and the Identification and Analysis of Clay Minerals*,
826 Oxford University Press, New York, 378 pp., ISBN 0 19 508713 5, 1997.
- 827 Morettini, E., Santantonio, M., Bartolini, A., Cecca, F., Baumgartner, P.O., and Hunziker, J.C.: Carbon isotope
828 stratigraphy and carbonate production during the Early–Middle Jurassic: examples from the Umbria–Marche–
829 Sabina Apennines (central Italy), *Palaeogeogr. Palaeocl.*, 184(3 – 4), 251 – 273, [https://doi.org/10.1016/S0031-](https://doi.org/10.1016/S0031-0182(02)00258-4)
830 [0182\(02\)00258-4](https://doi.org/10.1016/S0031-0182(02)00258-4), 2002.
- 831 Munier, T., Deconinck, J.F., Pellenard, P., Hesselbo, S.P., Riding, J.B., Ullmann, C.V., Bougeault, C.,
832 Mercuzot, M., Santoni, A.L., Huret, É. and Landrein, P.: Million-year-scale alternation of warm–humid and
833 semi-arid periods as a mid-latitude climate mode in the Early Jurassic (late Sinemurian, Lurasian
834 Seaway), *Clim. Past*, 17(4), 1547 – 1566, <https://doi.org/10.5194/cp-17-1547-2021>, 2021.
- 835 Nikitenko, B.L.: The Early Jurassic to Aalenian paleobiogeography of the Arctic Realm: implication of
836 microbenthos (Foraminifers and Ostracodes), *Stratigr. Geol. Correl.*, 16(1), 59 – 80,
837 <https://doi.org/10.1007/s11506-008-1005-z>, 2008.
- 838 Nordt, L., Breecker, D., and White, J.: Jurassic greenhouse ice-sheet fluctuations sensitive to atmospheric CO₂
839 dynamics, *Nat. Geosci.*, 15(1), 54 – 59, <https://doi.org/10.1038/s41561-021-00858-2>, 2022.
- 840 Oboh-Ikuenobe, F.E., Obi, C.G., and Jaramillo, C.A.: Lithofacies, palynofacies, and sequence stratigraphy of
841 Palaeogene strata in Southeastern Nigeria, *J. Afr. Earth Sci.*, 41(1 – 2), 79 – 101,
842 <https://doi.org/10.1016/j.jafrearsci.2005.02.002>, 2005.
- 843 Petschick, R.: MacDiff 4.2.2, available at: <http://servermac.geologie.unfrankfurt.de/Rainer.html>, 2000.
- 844 Pieńkowski, G., Uchman, A., Ninard, K., and Hesselbo, S.P.: Ichnology, sedimentology, and orbital cycles in
845 the hemipelagic Early Jurassic Lurasian Seaway (Pliensbachian, Cardigan Bay Basin, UK), *Global Planet.*
846 *Change*, 207, 103648, <https://doi.org/10.1016/j.gloplacha.2021.103648>, 2021.
- 847 Porter, S.J., Selby, D., Suzuki, K., and Gröcke, D.: Opening of a trans-Pangaeian marine corridor during the
848 Early Jurassic: Insights from osmium isotopes across the Sinemurian–Pliensbachian GSSP, Robin Hood's Bay,
849 UK, *Palaeogeogr. Palaeocl.*, 375, 50 – 58, <https://doi.org/10.1016/j.palaeo.2013.02.012>, 2013.
- 850 Price, G.D.: The evidence and implications of polar ice during the Mesozoic, *Earth Sci. Rev.*, 48(3), 183 – 210,
851 [https://doi.org/10.1016/S0012-8252\(99\)00048-3](https://doi.org/10.1016/S0012-8252(99)00048-3), 1999.
- 852 Price, G.D., Baker, S.J., Van De Velde, J., and Clémence, M.E.: High-resolution carbon cycle and seawater
853 temperature evolution during the Early Jurassic (Sinemurian–Early Pliensbachian), *Geochem. Geophys. Geosy.*,
854 17(10), 3917 – 3928, <https://doi.org/10.1002/2016GC006541>, 2016.

855 Quesada, S., Robles, S., and Rosales, I.: Depositional architecture and transgressive–regressive cycles within
856 Liassic backstepping carbonate ramps in the Basque–Cantabrian Basin, northern Spain, *J. Geol. Soc.*, 162(3),
857 531 – 548, <https://doi.org/10.1144/0016-764903-041>, 2005.

858 Raucsik, B., and Varga, A.: Climato-environmental controls on clay mineralogy of the Hettangian–Bajocian
859 successions of the Mecsek Mountains, Hungary: an evidence for extreme continental weathering during the
860 early Toarcian oceanic anoxic event, *Palaeogeogr. Palaeoclimatol.*, 265(1 – 2), 1 – 13,
861 <https://doi.org/10.1016/j.palaeo.2008.02.004>, 2008.

862 Riding, J.B., Leng, M.J., Kender, S., Hesselbo, S.P., and Feist-Burkhardt, S.: Isotopic and palynological
863 evidence for a new Early Jurassic environmental perturbation, *Palaeogeogr. Palaeoclimatol.*, 374, 16 – 27,
864 <https://doi.org/10.1016/j.palaeo.2012.10.019>, 2013.

865 Robinson, S.A., Ruhl, M., Astley, D.L., Naafs, B.D.A., Farnsworth, A.J., Bown, P.R., Hugh, J.C., Lunt, D.J.,
866 O’Brien, C., Pancost, R.D., Markwick, P.J.: Early Jurassic North Atlantic sea-surface temperatures from TEX
867 86 palaeothermometry, *Sedimentology*, 64(1), 215 – 230, <https://doi.org/10.1111/sed.12321>, 2016.

868 Rogov, M.A., and Zakharov, V.A.: Jurassic and Lower Cretaceous glendonite occurrences and their implication
869 for Arctic paleoclimate reconstructions and stratigraphy, *Earth Science Frontiers*, 17(Special Issue), 345 – 347,
870 2010.

871 Rosales, I., Quesada, S., and Robles, S.: Paleotemperature variations of Early Jurassic seawater recorded in
872 geochemical trends of belemnites from the Basque–Cantabrian basin, northern Spain, *Palaeogeogr.*
873 *Palaeoclimatol.*, 203(3 – 4), 253 – 275, [https://doi.org/10.1016/S0031-0182\(03\)00686-2](https://doi.org/10.1016/S0031-0182(03)00686-2), 2004.

874 Rosales, I., Quesada, S., and Robles, S.: Geochemical arguments for identifying second-order sea-level changes
875 in hemipelagic carbonate ramp deposits, *Terra Nova*, 18(4), 233 – 240, <https://doi.org/10.1111/j.1365-3121.2006.00684.x>, 2006.

877 Ruebsam, W., and Al-Husseini, M.: Orbitally synchronized late Pliensbachian–early Toarcian glacio-eustatic
878 and carbon-isotope cycles, *Palaeogeogr. Palaeoclimatol.*, 577, 110562, <https://doi.org/10.1016/j.palaeo.2021.110562>,
879 2021.

880 Ruebsam, W., Mayer, B., and Schwark, L.: Cryosphere carbon dynamics control early Toarcian global warming
881 and sea level evolution, *Global Planet. Change*, 172, 440 – 453, <https://doi.org/10.1016/j.gloplacha.2018.11.003>,
882 2019.

883 Ruebsam, W., and Schwark, L.: Impact of a northern-hemispherical cryosphere on late Pliensbachian–early
884 Toarcian climate and environment evolution, *Geol. Soc. Spec. Publ. London*, 514(1), 359 – 385,
885 <https://doi.org/10.1144/SP514-2021-1>, 2021.

886 Ruebsam, W., Reolid, M., Sabatino, N., Masetti, D., and Schwark, L.: Molecular paleothermometry of the early
887 Toarcian climate perturbation, *Global Planet. Change*, 195, 103351,
888 <https://doi.org/10.1016/j.gloplacha.2020.103351>, 2020a.

889 Ruebsam, W., Thibault, N., and Al-Husseini, M.: Early Toarcian glacio-eustatic unconformities and
890 chemostratigraphic black holes, in: *Stratigraphy and Timescales*, edited by: Montenari, M., 629 – 676,
891 Academic Press, <https://doi.org/10.1016/bs.sats.2020.08.006>, 2020b.

892 Ruffell, A., McKinley, J.M., and Worden, R.H.: Comparison of clay mineral stratigraphy to other proxy
893 palaeoclimate indicators in the Mesozoic of NW Europe, *Philos. T. Roy. Soc. A*, 360(1793), 675 – 693,
894 <https://doi.org/10.1098/rsta.2001.0961>, 2002.

895 Ruhl, M., Hesselbo, S.P., Hinnov, L., Jenkyns, H.C., Xu, W., Riding, J.B., Storm, M., Minisini, D., Ullmann,
896 C.V., and Leng, M.J.: Astronomical constraints on the duration of the Early Jurassic Pliensbachian Stage and
897 global climatic fluctuations, *Earth Planet. Sc. Lett.*, 455, 149 – 165, <https://doi.org/10.1016/j.epsl.2016.08.038>,
898 2016.

899 Ruvalcaba Baroni, I., Pohl, A., van Helmond, N.A., Papadomanolaki, N.M., Coe, A.L., Cohen, A.S., van de
900 Schootbrugge, B., Donnadieu, Y., and Slomp, C.P.: Ocean circulation in the Toarcian (Early Jurassic): a key
901 control on deoxygenation and carbon burial on the European Shelf, *Paleoceanography and*
902 *Paleoclimatology*, 33(9), 994 – 1012, <https://doi.org/10.1029/2018PA003394>, 2018.

903 Schweigert, G.: The occurrence of the Tethyan ammonite genus *Meneghiniceras* (Phylloceratina:
904 *Juraphyllitidae*) in the Upper Pliensbachian of SW Germany, *Stuttgarter Beiträge zur Naturkunde Serie B*
905 *Geologie und Paläontologie*, 356, 1 – 15, 2005.

906 Scott, A.C.: Charcoal recognition, taphonomy and uses in palaeoenvironmental analysis, *Palaeogeogr.*
907 *Palaeocl.*, 291(1 – 2), 11 – 39, <https://doi.org/10.1016/j.palaeo.2009.12.012>, 2010.

908 Sellwood, B.W., and Jenkyns, H.G.: Basins and swells and the evolution of an epeiric sea:(Pliensbachian–
909 Bajocian of Great Britain), *J. Geol. Soc.*, 131(4), 373 – 388, <https://doi.org/10.1144/gsjgs.131.4.0373>, 1975.

910 Sha, J.: Opening time of the Hispanic Corridor and migration patterns of pan-tropical cosmopolitan Jurassic
911 pectinid and ostreid bivalves, *Palaeogeogr. Palaeocl.*, 515, 34 – 46,
912 <https://doi.org/10.1016/j.palaeo.2018.09.018>, 2019.

913 Silva, R.L., Duarte, L.V., Comas-Rengifo, M.J., Mendonça Filho, J.G., and Azerêdo, A.C.: Update of the carbon
914 and oxygen isotopic records of the Early–Late Pliensbachian (Early Jurassic, ~ 187 Ma): Insights from the
915 organic-rich hemipelagic series of the Lusitanian Basin (Portugal), *Chem. Geol.*, 283(3 – 4), 177 – 184,
916 <https://doi.org/10.1016/j.chemgeo.2011.01.010>, 2011.

917 Silva, R.L., Duarte, L.V., Wach, G.D., Ruhl, M., Sadki, D., Gómez, J.J., Hesselbo, S.P., Xu, W., O'Connor, D.,
918 Rodrigues, B., and Mendonça Filho, J.G.: An Early Jurassic (Sinemurian–Toarcian) stratigraphic framework for
919 the occurrence of Organic Matter Preservation Intervals (OMPIs), *Earth Sci. Rev.*, 221, 103780,
920 <https://doi.org/10.1016/j.earscirev.2021.103780>, 2021.

921 Slater, S.M., Bown, P., Twitchett, R.J., Danise, S., and Vajda, V.: Global record of “ghost” nanofossils reveals
922 plankton resilience to high CO₂ and warming, *Science*, 376(6595), 853 – 856,
923 <https://doi.org/10.1126/science.abm73>, 2022.

- 924 Smith, P.L.: The Pliensbachian ammonite *Dayiceras dayiceroides* and early Jurassic paleogeography, *Can. J.*
925 *Earth Sci.*, 20(1), 86 – 91, <https://doi.org/10.1139/e83-008>, 1983.
- 926 Steinhorsdottir, M., and Vajda, V.: Early Jurassic (late Pliensbachian) CO₂ concentrations based on stomatal
927 analysis of fossil conifer leaves from eastern Australia, *Gondwana Res.*, 27(3), 932 – 939,
928 <https://doi.org/10.1016/j.gr.2013.08.021>, 2015.
- 929 Storm, M.S., Hesselbo, S.P., Jenkyns, H.C., Ruhl, M., Ullmann, C.V., Xu, W., Leng, M.J., Riding, J.B., and
930 Gorbanenko, O.: Orbital pacing and secular evolution of the Early Jurassic carbon cycle, *P. Natl. Acad. Sci.*
931 *USA*, 117(8), 3974 – 3982, <https://doi.org/10.1073/pnas.1912094117>, 2020.
- 932 Suan, G., Mattioli, E., Pittet, B., Lécuyer, C., Suchéras-Marx, B., Duarte, L. V., Philippe, M., Reggiani, L., and
933 Martineau, F.: Secular environmental precursors to Early Toarcian (Jurassic) extreme climate changes, *Earth*
934 *Planet. Sc. Lett.*, 290(3 – 4), 448 – 458, <https://doi.org/10.1016/j.epsl.2009.12.047>, 2010.
- 935 Suan, G., Nikitenko, B.L., Rogov, M.A., Baudin, F., Spangenberg, J.E., Knyazev, V.G., Glinskikh, L.A.,
936 Goryacheva, A.A., Adatte, T., Riding, J.B., Föllmi, K.B., Pittet, B., Mattioli, E., and Lécuyer, C.: Polar record
937 of Early Jurassic massive carbon injection, *Earth Planet. Sc. Lett.*, 312(1 – 2), 102 – 113,
938 <https://doi.org/10.1016/j.epsl.2011.09.050>, 2011.
- 939 Tappin, D.R., Chadwick, R.A., Jackson, A.A., Wingfield, R.T.R., and Smith, N.J.P.: *Geology of Cardigan Bay*
940 *and the Bristol Channel, United Kingdom offshore regional report*, British Geological Survey, HMSO, 107 pp,
941 ISBN 0 11 884506 3, 1994.
- 942 Thibault, N., Ruhl, M., Ullmann, C.V., Korte, C., Kemp, D.B., Gröcke, D.R., and Hesselbo, S.P.: The wider
943 context of the Lower Jurassic Toarcian oceanic anoxic event in Yorkshire coastal outcrops, UK, *Proceedings of*
944 *the Geologists' Association*, 129(3), 372 – 391, <https://doi.org/10.1016/j.pgeola.2017.10.007>, 2018.
- 945 Thiry, M.: Palaeoclimatic interpretation of clay minerals in marine deposits: an outlook from the continental
946 origin, *Earth Sci. Rev.*, 49(1 – 4), 201 – 221, [https://doi.org/10.1016/S0012-8252\(99\)00054-9](https://doi.org/10.1016/S0012-8252(99)00054-9), 2000.
- 947 Torsvik, T.H., and Cocks, L.R.M. (Eds.): *Jurassic*, in: *Earth History and Palaeogeography*, 208 – 218,
948 Cambridge University Press, 2017.
- 949 Ullmann, C.V., Szűcs, D., Jiang, M., Hudson, A.J., and Hesselbo, S.P.: Geochemistry of macrofossil, bulk rock,
950 and secondary calcite in the Early Jurassic strata of the Llanbedr (Mochras Farm) drill core, Cardigan Bay
951 Basin, Wales, UK, *J. Geol. Soc.*, 179(1), <https://doi.org/10.1144/jgs2021-018>, 2022.
- 952 Underhill, J.R., and Partington, M.A.: Jurassic thermal doming and deflation in the North Sea: implications of
953 the sequence stratigraphic evidence, Geological Society, London, *Petroleum Geology Conference series 4*, 337 –
954 345, <https://doi.org/10.1144/0040337>, 1993. van de Schootbrugge, B., Bailey, T.R., Rosenthal, Y., Katz, M.E.,
955 Wright, J D., Miller, K.G., Feist-Burkhardt, S., and Falkowski, P.G.: Early Jurassic climate change and the
956 radiation of organic-walled phytoplankton in the Tethys Ocean, *Paleobiology*, 31, 73–97,
957 [https://doi.org/10.1666/0094-8373\(2005\)0312.0.CO;2](https://doi.org/10.1666/0094-8373(2005)0312.0.CO;2), 2005.

- 958 van de Schootbrugge, B., Houben, A.J.P., Ercan, F.E.Z., Verreussel, R., Kerstholt, S., Janssen, N.M.M.,
959 Nikitenko, B., and Suan, G.: Enhanced arctic-tethys connectivity ended the toarcian oceanic anoxic event in NW
960 Europe, *Geol. Mag.*, 157(10), 1593 – 1611, <https://doi.org/10.1017/S0016756819001262>, 2019.
- 961 Waterhouse, H.K.: Orbital forcing of palynofacies in the Jurassic of France and the United Kingdom, *Geology*,
962 27(6), 511 – 514, [https://doi.org/10.1130/0091-7613\(1999\)027<0511:OFOPIT>2.3.CO;2](https://doi.org/10.1130/0091-7613(1999)027<0511:OFOPIT>2.3.CO;2), 1999.
- 963 Weedon, G.P.: Hemipelagic shelf sedimentation and climatic cycles: the basal Jurassic (Blue Lias) of South
964 Britain, *Earth Planet. Sc. Lett.*, 76(3 – 4), 321 – 335, [https://doi.org/10.1016/0012-821X\(86\)90083-X](https://doi.org/10.1016/0012-821X(86)90083-X), 1986.
- 965 Weedon, G.P., and Jenkyns, H.C.: Regular and irregular climatic cycles and the Belemnite Marls
966 (Pliensbachian, Lower Jurassic, Wessex Basin), *J. Geol. Soc.*, 147(6), 915 – 918,
967 <https://doi.org/10.1144/gsjgs.147.6.0915>, 1990.
- 968 Weedon, G.P., Page, K.N., and Jenkyns, H.C.: Cyclostratigraphy, stratigraphic gaps and the duration of the
969 Hettangian Stage (Jurassic): insights from the Blue Lias Formation of southern Britain, *Geol. Mag.*, 156(9),
970 1469 – 1509, <https://doi.org/10.1017/S0016756818000808>, 2019.
- 971 Woodland, A.W. (Ed.): The Llanbedr (Mochras Farm) Borehole, Institute of Geological Sciences, London,
972 Report No. 71/18, 115 pp., 1971.
- 973 Zakharov, V.A., Shurygin, B.N., Il'ina, V.I., and Nikitenko, B.L.: Pliensbachian-Toarcian biotic turnover in
974 north Siberia and the Arctic region, *Stratigr. Geol. Correl.*, 14(4), 399 – 417,
975 <https://doi.org/10.1134/S0869593806040046>, 2006.
- 976 Ziegler, P.A.: Geological Atlas of Western and Central Europe, 239, Shell Internationale Petroleum
977 Maatschappij, The Hague, 1990.
- 978